

1 Revision 3

2

3 **PARTIAL MELTING AND P-T EVOLUTION OF ECLOGITE-FACIES**
4 **METAPELITIC MIGMATITES FROM THE EGERE TERRANE (CENTRAL**
5 **HOGGAR, SOUTH ALGERIA)**

6 Amar Arab^{a, b*}, Gaston Godard^c, Khadidja Ouzegane^b, Antonio Acosta-Vigil^d, Jean-
7 Robert Kiénast, Manuel J. Román-Alpiste^d, Carlos J. Garrido^d, Amar Drareni^b

8 ^aFaculté SNVST, Université Akli Mohand Oulhadj, Bouira 10000, Algeria

9 ^bLaboratoire de Géodynamique, Géologie de l'Ingénieur et de Planétologie, FSTGAT-U.S.T.H.B., B.P. 32
10 El Alia, Dar el Beida, 16111-Alger, Algeria

11 ^cUniversité de Paris, Institut de Physique du Globe de Paris, CNRS, F-75005 Paris, France

12 ^dInstituto Andaluz de Ciencias de la Tierra, Consejo Superior de Investigaciones Científicas, Universidad
13 de Granada, Avenida de las Palmeras 4, 18100 Armilla, Granada, Spain

14 *corresponding author: a.arab@univ-bouira.dz

15 **ABSTRACT**

16 The Egéré terrane (Central Hoggar, South Algeria) includes mafic eclogite lenses
17 boudinaged in metapelitic rocks with high-pressure relicts. These metapelites show
18 textural records of partial melting, mainly primary melt inclusions enclosed in garnet
19 crystals and later crystallized as “nanogranitoids”. Garnet porphyroblasts also contain
20 inclusions of quartz, kyanite, phengite, biotite, staurolite and rutile, and show a smoothed
21 prograde zoning with a Mn bell-shaped profile. The peak high-pressure metamorphic
22 assemblage consists of garnet, kyanite, phengite (Si up to 6.36), quartz, rutile, \pm ilmenite,
23 \pm feldspars and melt. Phengite has partially transformed into fine-grained aggregates of
24 biotite, plagioclase and K-feldspar, a microstructure interpreted as resulting from a
25 dehydration melting during exhumation. Phengite breakdown, along with other
26 retrograde reactions, produced a late paragenesis with biotite, plagioclase, K-feldspar,
27 quartz, almandine-rich garnet, \pm sillimanite, \pm staurolite, \pm muscovite and ilmenite. The
28 thermodynamic modeling of P - T pseudosections allows to constrain various steps of the
29 metamorphic history: beginning of the garnet growth at 4.0 kbar and \sim 600°C during
30 prograde metamorphism; pressure peak at 14–20 kbar; temperature peak at 800–820°C;
31 formation of the last assemblage at 6.0–5.5 kbar and 725–685°C. Partial melting likely
32 started during the prograde path when crossing the H₂O-saturated solidus, at $T \geq 650$ –
33 670°C and $P \geq 10$ kbar, continued upon heating, up to the peak conditions, as well as
34 during decompression. This evolution is interpreted in terms of subduction of the
35 continental crust to mantle depths, followed by an exhumation through a clockwise P - T
36 path, during the Pan-African orogeny. The Egéré metapelites are relatively well-
37 preserved eclogite-facies rocks, contain inclusions of “nanogranitoids” hitherto very little

38 known in eclogite-facies metamorphic rocks, and represent an unusual trace of
39 subduction within a Neoproterozoic orogen.

40 **Keywords:** Hoggar, Egéré, high-pressure metapelites, phengite, partial melting,
41 nanogranitoids, pseudosections.

42 1. INTRODUCTION

43 The study of anatexis and *P-T* conditions of high-grade rocks is fundamental for
44 understanding the geodynamic evolution and rheological behavior of the continental
45 crust, particularly in convergent plate boundaries (*e.g.*, Rosenberg and Handy 2005).
46 Understanding the significance of anatexis requires the coupling of detailed petrological,
47 (micro)structural, geochemical and geochronological studies on migmatites.

48 This work combines two modern techniques to retrieve information on the
49 petrogenesis of Neoproterozoic anatectic continental crust exposed in the Hoggar orogen,
50 a Pan-African collisional belt extending from southern Algeria to northwestern Niger
51 (Black et al. 1994; Caby 2003; Liégeois et al. 2003): (a) thermodynamic modeling of *P-T*
52 pseudosections and (b) microstructural study of melt-bearing inclusions, including
53 nanogranitoids (*i.e.*, crystallized melt inclusions) and providing information on the
54 relative timing and nature of anatexis.

55 While melt inclusions are well-known to igneous petrologists and have been
56 extensively studied in subvolcanic and extrusive rocks, their occurrence in high-grade
57 metamorphic rocks of anatectic terranes is a novel and powerful research tool (Cesare et
58 al. 2009, 2015). Melt inclusions in migmatites and granulites are generally trapped by
59 peritectic minerals produced by incongruent melting reactions and, hence, represent
60 snapshots of primary anatectic melts (Cesare et al. 2009, 2015; Ferrero et al. 2012, 2018;
61 Bartoli et al. 2014, 2016). Although the study of melt inclusions in metamorphic rocks is
62 still in its infancy, those investigated so far indicate that the retrieved melt compositions
63 can be representative of the matrix melt present in the rock during entrapment (Acosta-
64 Vigil et al. 2010, 2012; Cesare et al. 2015; Bartoli et al. 2016).

65 An increasing number of high-grade metamorphic rocks have been recently
66 discovered and investigated from different localities in the Hoggar. Among them, rocks
67 that reached eclogite-facies conditions and preserved high-pressure (HP) parageneses are
68 particularly interesting because their study is essential to unravel the nature and evolution
69 of orogenic processes (*e.g.*, Berger et al. 2009, 2014; Doukkari et al. 2014, 2015; Adjerid
70 et al. 2015; Fettous 2016). To date, however, most of the reported and investigated HP
71 rocks are represented by metric to hectometric mafic eclogitic lenses. This study, in
72 contrast, investigates HP migmatitic metapelites of the Egéré-Aleksod terrane, Central
73 Hoggar, which are the first reported in the Hoggar with melt inclusions, now crystallized

74 into nanogranitoids. The principal goal of this contribution is elucidating the
75 metamorphic and anatexitic history of these migmatites, and their implications for the
76 history of the Egré terrane. This new data is combined with data from the surrounding
77 domains, to add new constraints on the eclogite-facies metamorphism in the Central
78 Hoggar and understand the geodynamic evolution of this orogenic belt.

79 **2. GEOLOGICAL BACKGROUND AND FIELD RELATIONSHIPS**

80 The Tuareg shield (S Algeria, W Mali and NW Niger) represents a Pan-African belt
81 located in between the West African Craton (WAC) to the west and the Saharan
82 metacraton to the east (Fig. 1). Formed by amalgamation of up to twenty-five terranes, it
83 is composed of Archean, Paleoproterozoic and juvenile Neoproterozoic rocks variably
84 reworked during the Pan-African orogeny (750–550 Ma; Black et al. 1994; Caby 2003;
85 Liégeois et al. 2003; Peucat et al. 2003; Liégeois et al. 2013; Liégeois 2019). According
86 to Liégeois et al. (1998), the long orogenic process includes a first major collision
87 between the Saharan metacraton and Eastern Hoggar terranes at ~750 Ma, marked by
88 major thrusts and the exhumation of HP metamorphic rocks. At around 650 Ma,
89 subduction and the maximum of tonalite-trondhjemite-granodiorite (TTG) magmatism
90 took place (Bechiri-Benmerzoug 2009). This episode produced HP metamorphism in the
91 Central Hoggar, the oblique collision of the Western Hoggar terranes with the WAC, and
92 northward migration of the Hoggar terranes along north-south shear zones, hundreds of
93 kilometers long (Bertrand and Caby 1978; Bertrand et al. 1986; Black et al. 1979; Caby
94 et al. 1989; Peucat et al. 2003). Later events, between 630 and 580 Ma, included high-
95 temperature (HT) regional metamorphism and the generation of high-K calc-alkaline
96 batholiths (Liégeois et al. 2003; Acef et al. 2003; Abdallah et al. 2007).

97 The polymetamorphic Central Hoggar is well-exposed at the core of the Tuareg
98 shield (Fig. 1a). It is made of eight terranes, delimited by shear zones: Laouni, Aouilène,
99 Tefedest, Egré-Aleksod, Azrou n’Fad, Assode-Issalane, Serouenout and Tazat (Black et
100 al. 1994). The first five are grouped under the “LATEA metacraton” acronym (Fig. 1b;
101 Liégeois et al. 2003, Liégeois 2019).

102 Lelubre (1952) and Duplan (1967, 1972) were the first to study the Egré-Aleksod
103 terrane, where Latouche (1985) described ortho- and para-derived rocks constituting
104 domes and basins, respectively. However, Doukkari et al. (2014, 2015), Doukkari (2016),
105 Arab et al. (2015) and Arab (2016) have considered the Egré terrane as composed of two
106 juxtaposed tectonic units separated by a mylonitic thrust, considered as a major tectonic
107 contact: (i) The Arechchoum basement made of migmatitic ortho- and para-gneisses
108 derived from Paleoproterozoic protoliths; (ii) the Egré meta-sedimentary cover, an
109 eclogite-facies unit made up mainly of kyanite-bearing metapelites (Fig. 2c-d) associated
110 with subordinate marbles, quartzites, several-meter-long lenses of mafic eclogite,

111 amphibolite and rare ultramafic rocks (Fig. 2a-b; Sautter 1985; Doukkari et al. 2014,
112 2015; Arab et al. 2015). In the investigated Izzilatène area, migmatites appear as
113 metatexites (Fig. 2d), and mafic eclogites constitute lenses within both migmatites and
114 marbles (Fig. 2a-b). Field observations, metamorphic constraints and U-Pb ages, as well
115 as geochemical data, suggest that the Egéré represents a former passive continental
116 margin intruded by mafic rocks, which afterwards was deeply subducted and then
117 exhumed (Arab 2016; Doukkari 2016; Ouzegane et al. in preparation).

118 3. PETROGRAPHY AND MINERAL CHEMISTRY

119 Representative metapelitic samples were collected from the Egéré meta-sedimentary
120 unit in the Izzilatène area, at the north of the Egéré terrane and ca. 50 km south of similar
121 rocks first reported by Arab et al. (2015) in the Tighsi area (Fig. 1b). In the field, these
122 metapelites appear as stromatic migmatites, with cm-to-mm-thick leucocratic bands
123 (leucosomes) alternating with darker bands rich in garnet and biotite, and parallel to the
124 main foliation. In hand specimen and under the microscope, they are banded rocks,
125 consisting of two petrographically different domains, leucosomes and melanosomes. The
126 leucosomes consist of quartz, feldspars and minor garnet. They are interspersed with
127 quartz-poor mafic melanosomes, which contain large garnet crystals, up to several
128 centimeters in diameter, together with kyanite, biotite, white micas, staurolite, sillimanite,
129 rutile and ilmenite (Fig. 2c-d).

130 Eight specimens of migmatitic metapelites (Table A in supplementary materials
131 [SM]) have been studied under the SEM and analyzed at the electron microprobe (see
132 methods in SM). They consist of variable proportions of garnet, kyanite, white micas
133 (phengite and muscovite), biotite, K-feldspar, plagioclase, quartz, staurolite and
134 sillimanite. Under the polarizing microscope, these rocks show a fine- to medium-grained
135 matrix made of quartz, feldspars, phengite, biotite, kyanite, sillimanite and staurolite,
136 which encloses cm-sized porphyroblasts of garnet and, less commonly, of kyanite (Fig. A
137 in SM). Accessory minerals are apatite, rutile, allanite, tourmaline, ilmenite and zircon.
138 These rocks often show an *augen*-like microstructure produced by large monocrystalline
139 quartz crystals or polycrystalline quartz aggregates (Fig. 3e), and/or large polymineralic
140 pseudomorphs after phengite (Figs. 3f, 4d-f; see below).

141 All the rocks sampled show comparable features; on the basis of microstructural
142 observations, the minerals have been grouped into the following three main metamorphic
143 parageneses.

144 (i) The earliest preserved assemblage (M_1) is represented by abundant mineral relicts
145 armored within garnet porphyroblasts (Grt_1), including quartz (Qz_1), biotite
146 (Bt_1), phengite (Ph_1), staurolite (St_1), kyanite (Ky_1), plagioclase (Pl_1), rutile
147 (Rt_1) and ilmenite (Ilm_1) (Figs. 3a-d, 4c).

- 148 (ii) The high-grade peak paragenesis (M_2) consists of the rims of the garnet
149 porphyroblasts (Grt_2) at contact with their matrix, made of kyanite (Ky_2),
150 phengite flakes (Ph_2), quartz (Qz_2), plagioclase (Pl_2), K-feldspar (Kfs_2),
151 apatite, rutile (Rt_2) and ilmenite (Ilm_2) (Fig. 4a). The minerals in the matrix,
152 mainly Qz_2 , Ph_2 and Ky_2 , define the main foliation in the rock. The
153 coexistence of melt with this paragenesis is discussed later.
- 154 (iii) A late assemblage (M_3) occurs either as a recrystallized matrix with biotite
155 (Bt_3), plagioclase (Pl_3), K-feldspar (Kfs_3), quartz (Qz_3), muscovite (Ms_3),
156 garnet (Gt_3), sillimanite (Sil_3), ilmenite (Ilm_3) and/or staurolite (St_3) (Figs.
157 3g-h, 4d), or as fine-grained symplectites made up of Bt_3 , Pl_3 and Kfs_3 (Fig.
158 4e-f), which formed mostly after Grt_{1-2} and Ph_2 .

159 In the following subsections, we describe the microstructure and composition of the
160 main minerals, whose analyzes are summarized in Tables B-F (SM).

161 3.1. Garnet

162 Three generations of garnet have been distinguished on the basis of microstructures
163 and compositions. The first two generations (Grt_{1-2}) correspond to the core and rims,
164 respectively, of euhedral to subhedral porphyroblasts, ~0.4 to 7 cm in diameter. These
165 porphyroblasts are well preserved, except some rims that appear partially replaced by
166 fine-grained Bt_3+Pl_3 aggregates (Figs. 3a, 4b). These Grt_{1-2} crystals are crowded with
167 mono- and poly-crystalline inclusions, which often define an either straight (Fig. 4c, e, g
168 in SM), sigmoid or spiral (Fig. 4b) internal foliation, at variable angles with respect to
169 the foliation in the matrix but occasionally in continuity with it, indicating that the garnet
170 porphyroblasts grew before or during the main deformation event. Some inclusions are
171 large (0.5–1.5 mm), anhedral, and consist of either individual or polycrystalline
172 inclusions of Qz_1 , Ph_1 , Bt_1 , St_1 , Rt_1 , Ilm_1 and/or zircon (Fig. 3b-d). Others, from 0.1 to 0.5
173 mm in size, are characterized by the presence of a thin optically-continuous moat of
174 plagioclase surrounding quartz (Pl in Figs. 3c, 4c). There are also small (~5–30 μm)
175 polymineral inclusions with the negative shapes of the host garnet (Fig. 5), which have all
176 the characteristics of nanogranitoids (Cesare et al. 2015). The largest polymineral
177 inclusions are visible mainly in the mantle and rim of the garnet porphyroblasts, while the
178 nanogranitoids are apparently distributed throughout the entire crystals. Sometimes,
179 garnet is also skeletal and appears intergrown with quartz (Fig. 3e).

180 Garnet porphyroblasts are rich in almandine ($Alm_{83-65}Prp_{4-13}Grs_{26-8}Sps_{6-0}$: Fig. 6a-d;
181 Table B in SM). In most of the samples, they show profiles characterized, from core to
182 rims, by decreases in X_{Grs} , X_{Sps} and X_{Fe} and an increase in X_{Prp} (Fig. 6a-d). A late
183 compositional zoning, with increases in X_{Fe} , X_{Sps} and X_{Grs} , and a decrease in X_{Prp} (Fig.
184 6c), is observed in the outer rims that are corroded by a late Bt_3+Pl_3 symplectite.

185 Grt₃ is observed as small crystals either scattered in the matrix, in association with
186 Bt₃, Pl₃, St₃ and sometimes Sil₃, or close to the large Grt₁₋₂ porphyroblasts, of which they
187 can represent modified relics of their resorbed rims. Compared with Grt₁, Grt₃ is richer in
188 Fe and poorer in Ca (Table B), having a very low grossular content ($X_{Grs} = 0.06-0.12$)
189 and a fairly high X_{Fe} (0.88–0.94), similarly to the retrograde outer rims of some corroded
190 garnet porphyroblasts (Fig. 6c-d).

191 3.2. White micas

192 Three generations of white mica have been observed. Phengite Ph₁ appears as rare
193 inclusions in the garnet porphyroblasts. Phengite Ph₂, by far the most abundant, occurs in
194 the matrix as large flakes, ~0.5–3.0 mm long, defining the main foliation; it therefore
195 developed before and/or during the main deformation event. These large crystals
196 frequently show Bt₃ and Ilm₃ lamellae, exsolved preferentially parallel to the (001)
197 cleavage (Figs. 3f, 4e-f). Ilm₃ exsolution lamellae are particularly abundant in the vicinity
198 of pre-existing Ilm₂ crystals (1 *in* Fig. 4f), suggesting that the initial Ph₂ was more
199 titaniferous here. Ph₂ flakes are partially or totally replaced by fine-grained symplectitic
200 aggregates of Bt₃+Pl₃, bounded by a continuous Kfs₃ corona at contact with Qz₂ (Fig. 4f)
201 and by a Pl₃+Ilm₃ symplectite around Ilm₂ (2 *in* Fig. 4f). Similar pseudomorphs after
202 phengite, observed elsewhere, are generally interpreted as formed during exhumation
203 (*e.g.*, Indares and Dunning 2001; Korhonen and Stout 2005; Lang and Gilotti 2007;
204 Dokukina et al. 2017). The third generation of white mica consists of small grains (0.1–
205 0.3 mm) of muscovite Ms₃, some of which are by-products of the Ph₂ breakdown, being
206 isolated in the Bt₃+Pl₃ symplectites (Figs. 3f, 4f).

207 White micas in most microstructural settings have a phengitic composition, though
208 with various Si contents (Fig. 4e; Table C in SM). Ph₁ is poorly substituted (Si ≈ 6.25
209 a.p.f.u.). The Ph₂ flakes are zoned, showing a decrease in phengite substitution from core
210 to rims: Si = 6.44 a.p.f.u. at core *vs.* 6.05 at rim; Al^t = 4.96 *vs.* 5.76; Ti = 0.17 *vs.* 0.08;
211 (Mg + Fe) = 0.51 *vs.* 0.22. The initial composition of a Ph₂ zone rich in Ilm₃ exsolution
212 lamellae (1 *in* Fig. 4f) was reconstructed at the electron microprobe by scanning ~100-
213 μm² adjacent areas with the electron beam during acquisition; the average composition
214 (Ti-Ph *in* Table C) suggests that Ph₂ before exsolution was here strongly substituted by
215 the theoretical end-member Ti-Fe-phengite (~1/3 of K₂Fe₂Ti₂[Si₆Al₂]O₂₀(OH)₄;
216 Auzanneau et al. 2010). Ms₃ in the Bt₃-Pl₃ pseudomorphs after phengite Ph₂ is similar in
217 chemistry to individual Ms₃ grains present in the rock matrix (Table C; Fig. 4e; Si =
218 5.96–6.05 a.p.f.u.; Ti = 0.03–0.12; [Mg + Fe] = 0.16–0.20) and to the rims of Ph₂ flakes,
219 suggesting that the zoning of the latter is linked to the formation of the Bt₃-Pl₃
220 symplectite and thus to retrogression.

221 3.3. Biotite

222 Biotite occurs in four main microstructural varieties: (i) As inclusions in garnet (Bt₁:
223 Fig. 3b). (ii) In the rock matrix, associated with Pl₃, Kfs₃ or St₃. Commonly, these biotite-
224 rich aggregates are fairly coarse-grained and oriented according to the main foliation
225 (Figs. Ac in SM, 3g bottom), but they sometimes show a gradual transition with fine-
226 grained unoriented Bt₃+Kfs₃+Pl₃ aggregates after Ph₂ (Fig. 3g upwards). Therefore,
227 biotite in the matrix is a post-peak Bt₃, the size and orientation of which depend on when
228 it formed relative to the main deformation event. (iii) Bt₃ is also intergrown Sil₃ (Fig. 3h).
229 (iv) Finally, minute Bt₃ lamellae parallel to the (001) plane of Ph₂ resulted from late
230 exsolution (Fig. 4e-f).

231 The large oriented biotite flakes in the matrix are unzoned, more magnesian ($X_{Fe} =$
232 0.40–0.54) and lower in Ti (≤ 0.34 a.p.f.u.) with respect to biotite from the fine-grained
233 aggregates in the matrix (Bt₃: $X_{Fe} = 0.67$ – 0.87 ; Ti = 0.36–0.48 a.p.f.u.) (Fig. 6g; Table D
234 in SM). Biotite exsolution lamellas in phengite are similar to biotite in the pseudomorphs
235 after Ph₂ (Bt₃; $X_{Fe} = 0.66$ – 0.69 ; Ti = 0.32–0.34 a.p.f.u.) (Fig. 4f; Table D).

236 3.4. Feldspars

237 K-feldspar (Or_{99–84}Ab_{1–15}An_{0–2}; Fig. 6h; Table E in SM) is widespread and, in most
238 cases, present in the leucosome. Late K-feldspar (Kfs₃) occurs in the late Bt₃-rich
239 aggregates and as coronae enveloping quartz at the former Qz₂-Ph₂ boundaries (Fig. 4e-
240 f).

241 The rare plagioclase crystals (0.1 mm) present in the leucosomes are relatively
242 homogeneous, with X_{An} ranging from 0.29 to 0.33 (Fig. 6h; Table E). The thin plagioclase
243 coronae surrounding Qz₁ inclusions in garnet are oligoclase (An_{14–15}; Fig. 3c; Table E).
244 The plagioclase Pl₃ associated with Bt₃, St₃ and/or Sil₃ in the matrix, and produced
245 essentially from Ph₂ (Fig. 4e-f), is An_{14–26} (Table E), whereas Pl₃ in the Bt₃-rich
246 aggregates that replaced garnet porphyroblasts (Figs. 3a, 4b) is slightly richer in anorthite
247 (An_{25–41}), due to the Ca content of garnet from which it grew.

248 3.5. Other minerals

249 Kyanite is observed as inclusions in garnet (Ky₁) and as large laths in the matrix
250 (Ky₂), ranging in size from ~0.1 mm to 2 cm, which, together with micas and quartz,
251 defines the main foliation (Fig. Ag in SM). Ky₂ may appear partially or completely
252 transformed to mm-sized bundles of fibrolitic sillimanite (Sil₃). Sil₃ appears also
253 intimately intergrown with Bt₃ as sheaf-like clusters (Fig. 3h).

254 Staurolite occurs both as inclusions in Grt₁ porphyroblasts (St₁ in Fig. 3c-d; $X_{Mg} =$
255 0.13–0.15; Si = 7.4–7.6 a.p.f.u.; TiO₂ = 0.64–0.87 wt%) and in the matrix associated with
256 Bt₃, Kfs₃, Pl₃, Gt₃ and Sil₃, as small scattered subhedral crystals (St₃ in Fig. 3g-h; $X_{Mg} =$
257 0.06–0.10; Si = 6.65–7.37 a.p.f.u.; TiO₂ = 0.49–0.74 wt%), with a more intense yellow

258 pleochroism. Clear $\text{Si}_{-1}\text{Al}^{\text{IV}}_{+1}\text{Al}^{\text{VI}}_{+1}\text{Fe}_{-1}$ (*i.e.*, Tschermak) and $\text{Mg}_{+1}\text{Fe}_{-1}$ substitutions are
259 observed in the analyzed staurolites (Fig. 6f; Table F in SM).

260 Rutile largely replaced by ilmenite, fluorapatite, allanite, zircon and tourmaline are
261 accessory minerals.

262 4. MICROSTRUCTURAL EVIDENCE OF PARTIAL MELTING

263 There are typical microstructures indicating the former presence of melt during high-
264 grade metamorphism, provided that crystallized and/or solidified melt has not been
265 affected by subsequent subsolidus deformation and recrystallization phenomena. The
266 most obvious are those present in shallow contact metamorphic aureoles, where melt has
267 either solidified into glass or crystallized into a granophyric intergrowth. Former melt
268 commonly constitutes thin films in between most crystals, and may include anhedral
269 reactant and/or euhedral peritectic minerals (Holness and Sawyer 2008).

270 The presence of melt is not so obvious in slowly cooled contact and regional
271 anatectic rocks (Sawyer 2001). There is a consensus however that several microstructures
272 are diagnostic: (i) subhedral to euhedral shapes, particularly for minerals that do not
273 typically produce crystal faces in metamorphic rocks (Vernon and Collins 1988); (ii) melt
274 pseudomorphs, identified by quartz or K-feldspar or sodic plagioclase, forming either
275 strongly cusped grains or thin films between other crystals (Harte et al. 1991; Clemens
276 and Holness 2000; Sawyer 2001; Marchildon and Brown 2002; Holness and Sawyer
277 2008); (iii) structures indicative of melt-producing reactions, like euhedral peritectic
278 minerals, anhedral relicts of reactant minerals surrounded by melt pseudomorphs,
279 oscillatory zoning, symplectitic coronae of Bt + Pl or Bt + Qz around ferromagnesian
280 crystals (Sawyer 1999; Vernon and Collins 2011); (iv) magmatic flow orientation
281 underlined by undeformed euhedral elongated crystals (Paterson et al. 1989; Sawyer
282 2001; Vernon and Collins 2011).

283 In the case of the studied Egéré metapelites, the first indications of the presence of
284 melt are based on field observations of leucosomes parallel to the main foliation. Under
285 the microscope, the leucosomes appear made of quartz with subhedral to euhedral
286 crystals of sodic plagioclase and K-feldspar. The presence of several types of mineral
287 intergrowths also points to the presence of melt: (i) Bt_3+Pl_3 aggregates around garnet
288 (Figs. 3a, 4b), interpreted by some authors as resulting from the breakdown of garnet
289 during cooling and melt crystallization (Janák et al. 1999); (ii) skeletal garnet intergrown
290 with quartz (Fig. 3e), interpreted as related either to prograde dehydration during melting
291 reactions or to a back-reaction with melt (Waters and Whales 1984; Waters 1988, 2001;
292 Vernon and Collins 1988; Powell and Downes 1990); (iii) Sil_3+Bt_3 sheaf-like
293 intergrowths (Fig. 3h), interpreted as products of a melt-residuum back-reaction (Dusel
294 and Foster 1983).

295 Strong microstructural evidence of the former presence of melt in high-grade
296 metamorphic rocks is also provided by some polycrystalline inclusions in garnet (*e.g.*,
297 Hartel et al. 1990; Perchuk et al. 2005; Lang and Gilotti 2007; Cesare et al. 2009, 2015).
298 Cesare et al. (2009, 2015) described what they termed “nanogranitoids”, referring to tiny
299 polycrystalline inclusions, up to a few tens of micrometers in size, representing
300 crystallized droplets of primary anatectic melt, trapped by the host peritectic mineral
301 growing during an incongruent melting reaction. Lang and Gilotti (2007) described
302 relatively large and mostly anhedral inclusions in garnet, consisting of mono- or poly-
303 crystalline quartz rimmed by a discontinuous moat of plagioclase and K-feldspar. They
304 interpreted this microstructure as representing a crystallized melt from the matrix, which
305 infiltrated or invaded the garnet crystals along cracks or grain boundaries, probably
306 during the expansion due to the transformation into quartz of former coesite inclusions
307 (see also the crown-like wavy microstructure of Korsakov and Hermann, 2006). On the
308 basis of experiments on inclusion-bearing garnet crystals from mafic eclogites, Perchuk
309 et al. (2005) showed that some large polycrystalline inclusions with melt-bearing
310 microstructures could be produced by the post-entrapment melting of former solid
311 polycrystalline inclusions involving hydrous minerals.

312 In the specific case of the Egéré migmatites, all three types of polycrystalline
313 inclusions are present in garnet and demonstrate anatexis of the host rock:

314 (i) *Nanogranitoids*: These inclusions are very small (~5–30 μm), equant, and
315 show the negative crystal forms of the host garnet (Fig. 5). They are rare and
316 scattered throughout the garnet porphyroblasts. These inclusions are
317 composed of quartz, biotite, plagioclase, K-feldspar, chlorite and accessory
318 minerals such as zircon and allanite. Given their distribution, size, shape and
319 mineralogy, they are interpreted as nanogranitoids. While zircon and allanite
320 would constitute solid inclusions entrapped with the melt, quartz, feldspars
321 and biotite probably represent daughter minerals crystallized from the trapped
322 melt; chlorite may be a low-*T* mineral formed during the retrograde *P-T* path.

323 (ii) *Inclusions of quartz surrounded by a thin feldspar moat*: Very similar to
324 those described by Lang and Gilotti (2007), these inclusions are subhedral to
325 euhedral, ~0.1–0.5 mm in size (Figs. 3c, 4c), and made up of mono- or poly-
326 crystalline quartz (Qz_1) in the center, rimmed by a thin moat of plagioclase,
327 either optically continuous or sometimes polycrystalline (Fig. 4c), which
328 suggest the former presence of melt (Sawyer 2001; Lang and Gilotti 2007).
329 Although these inclusions have been observed mainly at the rims of garnet
330 porphyroblasts, the secondary infiltration of matrix melt might not be the only
331 explanation for this particular microstructure; a primary mixture of reactants
332 and melt-crystallization products could be an alternative interpretation.

333 (iii) *Large polyphase inclusions*: About 0.5 to 1.5 mm in size, they consist of
334 quartz, feldspars, phengite, biotite, kyanite, staurolite, rutile and ilmenite, and
335 are found in the intermediate and rim regions of garnet porphyroblasts. They
336 could be interpreted as phengite-bearing polycrystalline inclusions that
337 partially melted after their entrapment in garnet (Perchuk et al. 2005). A more
338 detailed and specific study would however be necessary to confirm such an
339 origin.

340 5. PHASE EQUILIBRIA MODELING

341 In order to specify the metamorphic evolution of the metapelites, *P-T* pseudosections
342 (Fig. 7) were calculated using the software THERMOCALC (Powell and Holland 1988)
343 and an updated release of the thermodynamic dataset of Holland and Powell (2011) (see
344 method in SM for the details). To model the early prograde *P-T* evolution, we have
345 constructed a pseudosection for sample T78 (Fig. 7a). Results should however be
346 considered with caution, for two main reasons: (i) The early prograde evolution of a
347 pelitic metasediment takes place reasonably under conditions of H₂O saturation. As soon
348 as partial melting occurs, H₂O is strongly partitioned into the melt and the aqueous fluid
349 rapidly becomes absent in the system. The quantity of H₂O that has been considered for
350 modeling this early stage, higher than the loss-on-ignition value of the final rock, takes
351 these considerations into account, but is nevertheless arbitrary which causes large
352 uncertainties on the high-*T* part of Figure 7a. (ii) Some melt may have been lost from the
353 analyzed volume of the rock, and in part segregated to form the leucosomes (e.g., White
354 et al. 2004; Lasalle and Indares 2014). It would be wise to reintegrate a certain (arbitrary)
355 amount of melt into the modeled composition. We actually preferred considering a
356 sample large enough to include a representative amount of leucosome.

357 During partial melting, any water initially present dissolves into the melt (see above).
358 This is why it is better to calculate H₂O-undersaturated pseudosections to model the peak
359 and retrograde *P-T* evolution of these rocks, which we did using the bulk composition of
360 samples T52 and T78, of which the H₂O content was deduced from their loss-on-ignition
361 value (Fig. 7b-c; see Table A in SM for the compositions). A melanocratic part of sample
362 T52 was also separated and analyzed, in order to model a rock microdomain (Fig. 7d)
363 that mainly consists of Bt₃, St₃, Sil₃, Pl₃, Grt₃, quartz and ilmenite, which is considered to
364 be the most retrograde paragenesis.

365 6. DISCUSSION

366 On the basis of microstructural and mineralogical evidence, at least three distinct
367 stages of metamorphism have been recognized in the Eg er  metapelites: (i) the earliest
368 metamorphic stage (M₁) is prograde and documented by mineral inclusions enclosed in

369 garnet porphyroblasts; (ii) the peak eclogite-facies stage (M_2) developed a paragenesis
370 made of garnet, kyanite, phengite, quartz, rutile and melt; (iii) finally, the retrograde post-
371 peak stage (M_3) is highlighted by post-foliation minerals that developed in the matrix,
372 mainly as fine-grained pseudomorphs resulting from the breakdown of peak minerals like
373 phengite and garnet.

374 *6.1 Prograde evolution*

375 The prograde metamorphic evolution is documented by mineral inclusions preserved
376 in the core of garnet porphyroblasts (Grt_1), including Qz_1 , Ky_1 , Bt_1 , St_1 , Ph_1 , Rt_1 and Ilm_1
377 (Figs. 3a-d, 4c). Some of these inclusions exist alongside polycrystalline inclusions with
378 negative crystal shapes that are interpreted as nanogranitoids (Fig. 5), and thus testify to
379 the presence of a melt trapped in the host garnet during its growth (Section 4).

380 It is reasonable to assume that any initial prograde zoning in garnet would have been
381 smoothed or erased by diffusion at peak high-grade conditions (Spear and Florence 1992;
382 Caddick et al. 2010), which is corroborated here by the generally flat zoning pattern
383 observed in the core of the studied garnets (Fig. 6a, c). However, it is also well known
384 that bell-shaped X_{SpS} zoning profiles in garnet (e.g., samples T78, T138; Fig. 6a, c)
385 indicate prograde growth zoning (e.g., Tracy 1982; Loomis 1983; Mahar et al. 1997).
386 Likewise, the grossular content, higher in the core of garnet crystals than in their rims, is
387 also typical of a prograde growth zoning of garnet from metapelites (e.g., Woodsworth
388 1977; Chernoff and Carlson 1997; Keller et al. 2006). Overall, all these observations
389 suggest that Grt_1 grew at the expense of minerals now preserved as single mineral
390 inclusions, via reactions that occurred during the prograde evolution of the rock. At least
391 part of Grt_1 crystallized in the presence of melt, as shown by the presence of
392 nanogranitoids.

393 The prograde P - T trajectory was modeled by calculating a pseudosection for sample
394 T78 (Fig. 7), despite the uncertainties linked to such modeling (Section 5). Given the
395 high temperature reached by these rocks (800–820°C, see below), the initial prograde
396 zoning of garnet has been likely smoothed by diffusion at peak conditions. Hence, we did
397 not use garnet isopleths for modeling the prograde P - T path, which thus remains poorly
398 constrained. However, we tried to define a P - T evolution (red dashed arrow in Fig. 7a)
399 that explains both the growth of the garnet porphyroblasts (by crossing the garnet
400 isomodes: red dotted lines) and the entrapment of the various inclusions. An anchor
401 point, at ~600–630°C and ~6.0–6.5 kbar (blue ellipse in Fig. 7a), is provided by the
402 assemblage $Qz_1 + Bt_1 + Ph_1 + St_1 \pm Ky_1 + Pl + Ilm_1 (+Grt_1)$, shielded as inclusions in Grt_1
403 porphyroblasts of sample T78; it is further constrained by the intersection of Bt_1 and St_1
404 isopleths ($x(Bt) = 0.62$ – 0.64 ; $x(St) = 0.85$ – 0.88). To account for the presence of
405 "nanogranitoids" in garnet porphyroblasts, this early P - T evolution must have reached
406 fields of the pseudosection where melt ("Liq") is present and where the isomodes of

407 garnet are tightly spaced suggesting its peritectic growth (Fig. 7a). This could have
408 occurred during the crossing of the H₂O-saturated rock solidus at ca. $T \geq 650\text{--}670^\circ\text{C}$ and
409 $P \geq 10$ kbar. A modeled melt formed along the postulated trajectory at 10 kbar and
410 670°C , has the following composition: $\text{Si}_{39.84}\text{Al}_{10.15}\text{Fe}_{0.12}\text{Mg}_{0.06}\text{Ca}_{0.38}\text{Na}_{7.38}\text{K}_{1.69}\text{O}_{100}$ ·
411 $x\text{H}_2\text{O}$, which, after crystallization, would give a mineral assemblage compatible with the
412 nanogranitoids observed (Fig. 5; Section 4): 62.8 Pl (Ab₉₅) + 22.0 Qz + 13.8 Or + 1.4 Bt
413 (in vol.%; molar volumes from the Thermocalc database).

414 6.2 Peak *P-T* conditions

415 The prograde evolution should have continued towards the peak of metamorphism.
416 The H₂O-undersaturated pseudosections (Section 5) are used to constrain the peak or
417 near-peak *P-T* conditions (Fig. 7b-c). The peak assemblage (M₂) observed in the matrix
418 (Grt₂ + Ph₂ + Ky₂ + Qz₂ + Rt₂ + Ilm₂ + Kfs₂ + Pl₂ ± Liq) and whose feldspars are
419 concentrated in leucosomes, is stable over a large *P* range between 12 and 20 kbar. It is
420 therefore necessary to better define the peak conditions by using the isopleths of garnet
421 and/or phengite. In doing so, several drawbacks arise:

422 (i) The temperatures reached during the peak of metamorphism have produced a
423 significant, but incomplete, chemical homogenization of garnet porphyroblasts, with
424 almost flat zonation profiles except at their rim, which reequilibrated during the
425 retrograde metamorphism (Fig. 6a-d). Hence, it is appropriate to use the composition of
426 the large central parts of the garnet porphyroblasts to refine the peak *P-T* conditions.
427 However, the calculated X_{Fe} and X_{Grs} isopleths in garnet ($x(\text{Grt})$ and $z(\text{Grt})$ in Fig. 7b-c)
428 vary only very little over the large *P* range in which the paragenesis M₂ is stable, and are
429 thus of limited interest.

430 (ii) The composition of phengite seems more reliable because the isopleths $Si(\text{Ph})$,
431 related to the content in celadonite, are closely spaced (Fig. 7c-d), and can be applied to
432 the nearly homogeneous Ph₂ flakes. The measured values of Si in phengite suggest *P* >
433 14 kbar when compared with the calculated $Si(\text{Ph})$ isopleths ($Si(\text{Ph}) \pm 1\sigma$: 6.278 ± 0.038
434 [T78]; 6.234 ± 0.022 [T52]). High-grade conditions are also indicated by the Ti richness
435 of parts of Ph₂ (Section 3.2; Ti-Ph in Table C; e.g., Nahodilová et al. 2014; Auzanneau et
436 al. 2010).

437 (iii) The liquid produced by anatexis (Section 4) could have been partially extracted
438 from the rock, producing a change in composition of the system and a shift of the solidus
439 curve towards higher temperatures (dashed blue arrows in Fig. 7b-c). In the borderline
440 case where all melt is extracted, the solidus curve would shift and follow the *P-T*
441 conditions of the rock, since the solidus corresponds to those conditions where the melt
442 exists only in infinitesimal amount. It is unlikely, however, that all of the melt was
443 extracted because a critical threshold of liquid is required for melt interconnection and

444 migration (<1 to a few vol.%; Laporte and Watson 1995; Laporte et al. 1997; Rosenberg
445 and Handy 2005). Consequently, the modeled pseudosections of Figure 8b-c give a
446 "snapshot" that probably approaches but does not reach this borderline case. They would
447 reflect the situation close to the T peak, and are thus poorly suited for determining the
448 conditions prior to it.

449 The P peak must have been reached at lower temperatures relative to the ultimate
450 solidus curve given by the pseudosections, in the stability field of the M_2 paragenesis (Grt
451 + Ph + Ky + Qz + Ilm \pm Rt + Kfs + Pl), and in the wide range of P between 14 and 20
452 kbar given with great uncertainty by the garnet and phengite isopleths (Fig. 7b-c). Some
453 constraints, like Ph₂ still abundant in the rock, together with feldspars and melt, and the
454 location of the ultimate solidus curve, suggest a subsequent T peak at about 800–820°C.
455 The Ti-in-Zrn thermometry applied to similar neighboring metapelites yielded peak
456 temperatures of $811 \pm 15^\circ\text{C}$ (Bruguier et al. 2014). The P - T trajectories drawn in Figure
457 8b-c are an attempt to represent this imperfectly constrained evolution.

458 *6.3 Retrograde evolution*

459 The P - T trajectory of exhumation is documented by the M_3 paragenesis, made of
460 abundant Bt₃, Pl₃, Kfs₃ and quartz, scarce Sil₃, Ms₃, Grt₃, \pm St₃ and Ilm₃. The M_3
461 assemblage often forms unoriented fine-grained polymineralic aggregates (almost
462 symplectites) and therefore postdates the main foliation. In some specimens, however,
463 Bt₃ shows a significant orientation (Section 3.3; Fig. 3g), indicating some deformation at
464 this stage. M_3 developed at the expense of previous M_2 minerals, mainly garnet and
465 phengite. Sillimanite and ilmenite also replaced kyanite and rutile, respectively.

466 The garnet porphyroblasts, largely homogenized at the peak of metamorphism (see
467 above), show a drop in X_{Fe} and X_{Grs} and an increase of X_{prp} at their rims ("rims" in Fig.
468 6a, c). Moreover, when they have been corroded by a fine-grained Bt₃+Pl₃ aggregate
469 (Fig. 4b), these porphyroblasts show slight increases of X_{Fe} and X_{Grs} at their very edges
470 ("outer rim" of Fig. 6c). Some small anhedral Grt₃ crystals, whose X_{Fe} is even greater
471 (Fig. 6d; Table B), may well be relicts of these porphyroblast edges, isolated during the
472 development of the replacing minerals. Many authors have interpreted such an increase in
473 X_{Fe} as resulting from Fe-Mg exchange between garnet and surrounding biotite during
474 retrogression (*e.g.*, Tracy et al. 1976; Woodsworth 1977; Tuccillo et al. 1990; Konrad-
475 Schmolke et al. 2005).

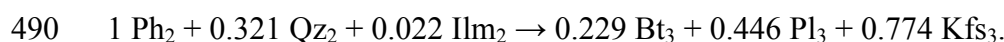
476 The phengite flakes in the matrix (Ph₂) have been partly or totally replaced by a fine-
477 grained Bt₃+Pl₃ aggregate, which is further rimmed by a Kfs₃ corona at contacts with Qz₂
478 (Figs. 3f, 4e-f). They show a chemical evolution towards the muscovite end-member
479 (Fig. 6e), mainly at their rims transformed into Bt₃+Pl₃. A few specks of Ms₃ (Figs. 4f
480 and 6e) isolated among Bt₃ and Pl₃ seem to be re-equilibrated relicts of Ph₂. Ilm₂ initially

481 in contact with Ph₂ is also rimmed by concentric coronas of Pl₃ and Bt₃ (2 in Fig. 4f), and
482 would have operated as a minor reactant, supplying some Ti (and Fe) to the newly
483 formed biotite, whose high Ti-content is likely related to HT metamorphic conditions
484 (e.g., Henry and Guidotti 2002).

485 The stoichiometric balance of the phengite breakdown reaction was made by the
486 least-squares method (sample T138; for 1 mol of Ph₂):



488 where *R* is the vector of the residuals (*R*: Si_{0.00}Al_{0.48}Cr_{+0.00}Ti_{-0.23}Fe_{+0.23}Mn.
489 0.00Mg_{+0.07}Ca_{+0.42}Na_{+0.80}K_{+0.47}O_{0.00}). The conversion into volumes yields:



491 The minerals are correctly distributed between reactants and products, in volumetric
492 proportions comparable to what is observed (Fig. 4f). The increase in volume during the
493 reaction ($\Delta V_s/V_s = +0.079$) is also consistent with an evolution at decreasing pressure.
494 However, associated residuals are abnormally important, indicating that some additional
495 exchange took place during the reaction, which therefore occurred in an open system with
496 respect to the reaction domain considered.

497 Indeed, such an exchange could be linked to a mobile melt. Fluid-absent melting of
498 phengite typically occurs during the decompression of HP metapelitic and felsic rocks
499 (e.g., Vielzeuf and Holloway 1988; Hermann and Green 2001; Schmidt et al. 2004;
500 Hermann et al. 2006; Massonne 2009; Dokukina et al. 2017). Phengite melting in the
501 studied rocks is consistent with the calculated *P-T* pseudosections, where the phengite-
502 out and solidus curves almost coincide (Fig. 7b-c). During the retrograde evolution, the
503 metapelites followed a *P-T* path sub-parallel to these two curves or, more likely, these
504 curves were shifted in the vicinity of the *P-T* path, by extraction of melt, as discussed
505 before (Section 6.2 iii). This evolution can explain the zonation observed at the rims of
506 both garnet porphyroblasts (decrease in *X_{Fe}* and *X_{Grs}*: Fig. 6a-d) and phengite flakes
507 (decrease in the celadonite end-member: Fig. 6e), which are consistent with the
508 decreasing values of *x(Grt)*, *z(Grt)* and *Si(Ph)* predicted by the pseudosections during a
509 drop of *P* (Fig. 7b-c).

510 The final step of decompression and cooling is manifested by the formation of M₃
511 fine-grained aggregates, indicating an evolution into the melt-free stability fields of
512 sillimanite and biotite (Fig. 7). Despite the tight spacing of isopleths in this region of the
513 pseudosections, the compositional heterogeneity of the M₃ domains and minerals, which
514 likely did not fully reach equilibrium, makes it difficult to specify the *P-T* conditions of
515 this late metamorphic stage. Garnets in contact with the matrix, either “outer rims” of
516 porphyroblasts or Grt₃, have the lowest grossular content [*z(Grt₃)*: 0.13–0.05 for sample

517 T78; 0.10–0.08 for T52] and the highest X_{Fe} ratio [$x(Grt_3)$: 0.85–0.91 for T78; 0.87–0.93
518 for T52]. The X_{Fe} isopleth values for Bt_3 are: $x(Bt_3) = 0.58–0.62$ for T78; 0.67–0.69 for
519 T52. The isopleths do not intersect at a point but in a P - T region that provides a
520 reasonable estimate for the conditions of this stage (blue ellipses in Fig. 7b-d): 725–
521 740°C at 7–8 kbar (T78); 720–730°C at 7.0–7.5 kbar (T52). Since equilibrium is
522 imperfectly achieved at the scale of the sample, we modeled a small homogeneous matrix
523 domain, similar to that of Figure 3g, for sample T52 (Fig. 7d). The compositions of the
524 minerals [$x(Grt_3)$: 0.87–0.88; $z(Grt_3)$: 0.05–0.06; $x(St_3)$: 0.89–0.94; $x(Bt_3)$: 0.62–0.71]
525 suggest P - T conditions of 5.5–6.0 kbar, 675–725°C (blue ellipse in Fig. 7d) on a regular
526 geothermal gradient of $\sim 15^\circ\text{C.km}^{-1}$. Moreover, modeling this microdomain reveals
527 features not shown by the bulk-rock pseudosection, like the local stability of St_3 and the
528 late increase of X_{Fe} in the garnet “outer rim” (see $x(Grt)$ isopleths in Fig. 7d).

529 6.4. Petrological and geological implications

530 The metapelites studied here are distinctive regarding three particular circumstances
531 that, combined, make these rocks a kind of “geological miracle”:

532 (i) *Eclogite-facies metapelites*. Eclogite-facies mafic metabasites, *i.e.*, true eclogites,
533 have been known for two centuries, but metapelites related to eclogites went unnoticed
534 for a long time, to the point that, in the 1980-90s, a controversy “foreign” vs. “in-situ”
535 raised the question of the relationships between eclogites and their metapelitic host, in
536 which traces of such metamorphism were not observed (see the historical summary *in*
537 Godard 2001). It has since been recognized that, among eclogite-facies rocks, metapelites
538 are not less rare than metabasites, but have rarely preserved their eclogite-facies imprint
539 due to the combined effects of retrograde metamorphism, rehydration and late
540 deformation. In this regard, the difficulty in specifying the P - T conditions prevailing at
541 the peak of metamorphism (Section 6.2) is usual for this type of rock. It remains that it is
542 amazing to observe in the Egéré terrane such rocks on a regional scale. Without wishing
543 to reignite the controversy, it should be noted that the mafic eclogites and eclogite-facies
544 metapelites from Egéré seem to have recorded slightly different P - T evolutions: In
545 Tighsi, 30–40 km N of the investigated Izzilatène area, the apparent P - T path of mafic
546 eclogites (19.6 kbar/695°C \rightarrow 15.5 kbar/775°C \rightarrow 9.3 kbar/695°C) does not exactly
547 superimpose on that of the host metapelites (17–19 kbar/850°C \rightarrow 9 kbar/750 °C)
548 (Doukkari et al. 2014; Arab et al. 2015). The same is observed in Izzilatène, between the
549 mafic eclogites (13–14 kbar/580°C \rightarrow 19 kbar/650–700 °C \rightarrow 8–9 kbar/700–750 °C:
550 Doukkari et al. 2015) and the investigated eclogite-facies metapelites (6.0–6.5 kbar/600–
551 630°C \rightarrow 14–20 kbar/800–820°C \rightarrow 5.5–6.0 kbar/675–725°C: this study). In both cases,
552 the apparent P peak is slightly lower, or at least less well defined, for the metapelites than
553 for the metabasites. On the other hand, the T peak seems higher by a hundred degrees for
554 metapelites compared with the mafic eclogite lenses that they contain. It is difficult to
555 imagine that these differences are linked to some major geological process. It makes

556 more sense to invoke a bias linked to thermodynamic modeling, or even more surely a
557 contrasting behavior of the two types of rock, since, relative to the metapelites, the
558 metabasites preserve more easily the imprint of the *P* peak but record less easily the *T*
559 peak because of their refractory properties.

560 (ii) *Nanogranitoids in eclogite-facies rocks*. Partial melting of eclogite-facies rocks is
561 still a matter of debate, not because melting under (ultra)high-pressure conditions is not
562 predicted by experiments and thermodynamics (e.g., Hermann et al. 2006), but because
563 of the lack of irrefutable petrological evidence, especially for mafic eclogites. There is a
564 score of microstructures that suggest partial melting in some eclogite-facies rocks (see
565 review in Section 4), but a compelling evidence like melt inclusions sheltered in garnet
566 and crystallized as “nanogranitoids” is rare. Such inclusions are well known in HT
567 granulite-facies migmatites (e.g., Cesare et al. 2009, 2015; Ferrero et al. 2012; Bartoli et
568 al. 2016), less frequently in HP granulite-facies rocks (Ferrero et al. 2018), and more
569 rarely in eclogite-facies quartzo-feldspathic rocks (Ferrero et al. 2015). This study
570 confirms that they exist under eclogite-facies conditions, despite less favorable
571 geotherms, although no evidence of melting has been found in the associated mafic
572 eclogites, likely because of their refractory composition.

573 (iii) *Eclogite-facies metamorphism in a Neoproterozoic orogen*. Recent studies (e.g.,
574 Doukkari et al. 2014, 2015; Arab et al. 2015; Arab 2016; and references therein) suggest
575 that the Egré supracrustal sequence deposited in a continental rift/passive margin
576 environment, at an age of ≥ 745 Ma. It has been suggested that these sediments were
577 intruded by mafic rocks and subducted deeply during the Neoproterozoic evolution of the
578 Hoggar, likely during the Upper Cryogenian-Lower Ediacarian (Liégeois et al. 2003;
579 Arab 2016), thus recording eclogite-facies conditions, before being exhumed. The LA-
580 ICP-MS U-Pb analysis of a zircon megacryst from a neighboring eclogite-facies
581 metapelite, crystallized from the anatectic melt at conditions close to the *T* peak, gave an
582 Upper Cryogenian age of 654 ± 5 Ma (Bruguier et al. 2014). The Egré terrane would
583 then represent an old passive margin that underwent a subduction-exhumation cycle
584 related to the Pan-African orogeny that led to the Western Gondwana assembly (Liégeois
585 et al. 2013; Berger et al. 2014; Liégeois 2019). The existence in the Hoggar of numerous
586 traces of an eclogite-facies metamorphism dating back to the Neoproterozoic is
587 remarkable, since the first true eclogites on Earth formed around 2.1 Ga ago (e.g., Loose
588 and Shenk 2018), indicating the emergence of modern plate tectonics. This type of
589 metamorphism remained quite rare in the Neoproterozoic, before gradually increasing
590 from the Paleozoic to the Present. The Egré terrane belongs to the West Gondwana
591 Orogen (WGO), which stretches from Hoggar to the northeast of Brazil and is
592 characterized by a Cryogenian-Ediacarian subduction, which Ganade de Araujo et al.
593 (2014) consider as the earliest evidence of large-scale deep continental subduction and
594 Himalayan-scale mountains in the geological record.

595 7. IMPLICATIONS

596 The studied migmatitic metapelites preserve mineral zoning and textures related to
597 various stages of their prograde and retrograde metamorphic evolution, and provide
598 constraints on partial melting reactions under HP conditions. The following conclusions
599 can be made:

600 1. The metasedimentary Egéré unit (LATEA terrane, Central Hoggar, Algeria)
601 mainly consists of kyanite-bearing metapelites, quartzites, marbles and mafic rocks that
602 have undergone eclogite-facies metamorphism.

603 2. The studied metapelites consist of quartz, garnet, phengite, kyanite, rutile, with
604 secondary biotite, staurolite, muscovite, K-feldspar, plagioclase, sillimanite and ilmenite.
605 Garnet porphyroblasts show smoothed bell-shaped zoning patterns, with spessartine and
606 grossular decreases from core to rim. They grew during prograde metamorphism,
607 enclosing quartz, biotite, phengite, staurolite, kyanite, rutile and ilmenite. Coarse-grained
608 minerals, namely phengite, quartz and kyanite, form a foliated matrix and, together with
609 the rims of euhedral garnet porphyroblasts, constitute the peak paragenesis. Fine-grained
610 matrix minerals, mostly unoriented, like biotite, plagioclase, K-feldspar, muscovite,
611 staurolite and sillimanite, developed during exhumation throughout retrograde reactions
612 that produced a variety of intergrowths, coronas and pseudomorphs.

613 3. Two types of melting phenomena have occurred in the studied rocks: (i) H₂O-
614 saturated melting during the prograde stage; and (ii) H₂O-unsaturated melting near the
615 peak and during decompression, likely associated with the dehydration melting of
616 phengite.

617 4. Polycrystalline micro-inclusions in garnet, with negative crystal shapes, formed
618 after entrapment of former melt and are therefore “nanogranitoids”. Together with quartz
619 inclusions surrounded by feldspar, they provide evidence for anatexis during the prograde
620 evolution. Anatexis close to the metamorphic *T* peak gave a migmatitic structure to the
621 rocks. Biotite-plagioclase-bearing pseudomorphs are linked to dehydration melting of
622 phengite during exhumation.

623 5. A clockwise *P-T* path is suggested for the Egéré metapelites, based on micro-
624 textures and *P-T* pseudosections. The recorded starting conditions of the prograde
625 evolution, evidenced from the mineral inclusions preserved in garnet, are 600–630°C and
626 6.0–6.5 kbar. The inferred peak assemblage (quartz, garnet, kyanite, phengite, rutile,
627 melt, ±plagioclase, ±K-feldspar) indicates a *P* peak of metamorphism at 14–20 kbar and a
628 *T* peak at 800–820°C. The assemblage garnet–biotite–staurolite–sillimanite–plagioclase–
629 K-feldspar–ilmenite, which occurs as late intergrowths, coronas and pseudomorphs,
630 formed at the expense of the HP paragenesis and documents the completion of the
631 retrograde evolution at ~6 kbar and 600–620°C.

632 6. The clockwise P - T path recorded by the Egéré HP metapelites is related to
633 continental subduction followed by exhumation during the Pan-African orogeny that led
634 to the amalgamation of the Hoggar shield. Recent geochronological data indicate that the
635 HP event likely took place at ~650 Ma.

636 7. The rocks studied are remarkable because (i) they are relatively well-preserved
637 eclogite-facies metapelites, (ii) they contain “nanogranitoids”, rarely described so far in
638 eclogite-facies metamorphic rocks, and (iii) they indicate a subduction-related
639 metamorphism during a Neoproterozoic orogeny.

640 **ACKNOWLEDGEMENTS**

641 This work is a contribution to the project PHC TASSILLI 15MDU943 and the FP7-
642 IRSES-612572 project “MEDYNA” funded under REA Grant Agreement
643 PIRSES-GA-2013-612572. We are extremely grateful to *Office du Parc National de*
644 *l’Ahaggar* (Tamanrasset, Algeria) for logistic support during fieldwork, to Chunjing Wei
645 and Abderrahmane Bendaoud for constructive reviews and to Fang-Zhen Teng for the
646 editorial work.

647 **REFERENCES**

- 648 Abdallah, N., Liégeois, J.-P., De Waele, B., Fezaa, N., and Ouabadi, A. (2007) The
649 Temaguessine Fe-cordierite orbicular granite (Central Hoggar, Algeria): U-Pb
650 SHRIMP age, petrology, origin and geodynamical consequences for the late Pan-
651 African magmatism of the Tuareg shield. *Journal of African Earth Sciences*,
652 49(4), 153-178.
- 653 Acef, K., Liégeois, J.P., Ouabadi, A., and Latouche, L. (2003) The Anfeg post-collisional
654 Pan-African high-K calc-alkaline batholith (Central Hoggar, Algeria), result of
655 the LATEA microcontinent metacratonization. *Journal of African Earth Sciences*,
656 37(3), 295-311.
- 657 Acosta-Vigil, A., Buick, I., Hermann, J., Cesare, B., Rubatto, D., London, D., and
658 Morgan, V.I.G.B. (2010) Mechanisms of crustal anatexis: a geochemical study of
659 partially melted metapelitic enclaves and host dacite, SE Spain. *Journal of*
660 *Petrology*, 51(4), 785-821.
- 661 Acosta-Vigil, A., Buick, I., Cesare, B., London, D., and Morgan, V.I.G.B. (2012) The
662 extent of equilibration between melt and residuum during regional anatexis and its
663 implications for differentiation of the continental crust: A study of partially
664 melted metapelitic enclaves. *Journal of Petrology*, 53(7), 1319-1356.
- 665 Acosta-Vigil, A., London, D., Morgan, G.B., Cesare, B., Buick, I., Hermann, J., and
666 Bartoli, O. (2017) Primary crustal melt compositions: Insights into the controls,
667 mechanisms and timing of generation from kinetics experiments and melt
668 inclusions. *Lithos*, 286–287, 454-479.

- 669 Adjerid, Z., Godard, G., Ouzzegane, K. (2015) High-pressure whiteschists from the Ti-N-
670 Eggoleh area (Central Hoggar, Algeria): a record of Pan-African oceanic
671 subduction. *Lithos*, 226, 201-216.
- 672 Arab, A. (2016) Les séries métasédimentaires de haute pression et les migmatites du
673 socle de l'Egéré (Nord Hoggar): télédétection, géochimie et relations de phases,
674 150 p. Ph.D. thesis, USTHB, Algiers.
- 675 Arab, A., Ouzegane, K., Drareni, A., Doukkari, S., Zetoutou, S., and Kiénast, J.-R.
676 (2015) Phase equilibria modeling of kyanite-bearing eclogitic metapelites in the
677 NCKFMASHTO system from the Egéré terrane (Central Hoggar, South Algeria).
678 *Arabian Journal of Geosciences*, 8(5), 2443-2455.
- 679 Auzanneau, E., Schmidt, M.W., Vielzeuf, D., Connolly, J.A.D. (2010) Titanium in
680 phengite: a geobarometer for high temperature eclogites. *Contributions to
681 Mineralogy and Petrology*, 159: 1. <https://doi.org/10.1007/s00410-009-0412-7>.
- 682 Bartoli, O., Cesare, B., Remusat, L., Acosta-Vigil, A., and Poli, S. (2014) The H₂O
683 content of granite embryos. *Earth and Planetary Science Letters*, 395, 281-290.
- 684 Bartoli, O., Acosta-Vigil, A., Ferrero, S., and Cesare, B. (2016) Granitoid magmas
685 preserved as melt inclusions in high-grade metamorphic rock. *American
686 Mineralogist*, 101(7), 1543-1559.
- 687 Bechiri-Benmerzoug, F. (2009) Pétrologie, géochimie isotopique et géochronologie des
688 granitoïdes Pan-Africains de type TTG de Silet: contribution à la connaissance de
689 la structuration du bloc d'Iskel (Silet, Hoggar occidentale), Algérie. Thèse de
690 Doctorat (USTHB/FSTGAT), Alger.
- 691 Berger, J., Caby, R., Liégeois, J.-P., Mercier, J.-C.C., and Demaiffe, D. (2009)
692 Dehydration, melting and related garnet growth in the deep root of the
693 Amalaoulaou Neoproterozoic magmatic arc (Gourma, NE Mali). *Geological
694 Magazine*, 146(2), 173-186.
- 695 Berger, J., Ouzegane, K., Bendaoud, A., Liégeois, J.-P., Kiénast, J.-R., Bruguier, O., and
696 Caby, R. (2014) Continental subduction recorded by Neoproterozoic eclogite and
697 garnet amphibolites from Western Hoggar (Tassendjanet terrane, Tuareg Shield,
698 Algeria). *Precambrian Research*, 247, 139-158.
- 699 Bertrand, J.M.L., and Caby, R. (1978) Geodynamic evolution of the Pan-African
700 orogenic belt: A new interpretation of the Hoggar shield (Algerian Sahara).
701 *Geologische Rundschau*, 67(2), 357-388.
- 702 Bertrand, J.-M., Michard, A., Boullier, A.-M., and Dautel, D. (1986) Structure and U/Pb
703 geochronology of Central Hoggar (Algeria): A reappraisal of its Pan-African
704 evolution. *Tectonics*, 5(7), 955-972.
- 705 Black, R., Caby, R., Moussine-Pouchkine, A., Bayer, R., Bertrand, J.M., Boullier, A.M.,
706 Fabre, J., and Lesquer, A. (1979) Evidence for late Precambrian plate tectonics in
707 West Africa. *Nature*, 278, 223.
- 708 Black, R., Latouche, L., Liégeois, J.P., Caby, R., and Bertrand, J.M. (1994) Pan-African
709 displaced terranes in the Tuareg shield (central Sahara). *Geology*, 22(7), 641-644.
- 710 Bruguier, O., Caby, R., Bendaoud, A., Bosch, D., Deloule, E., Kiénast, J.R., and
711 Ouzegane, K. (2014) Zircon megacryst from a Neoproterozoic eclogite of Central
712 Hoggar (Algeria): U-Pb, trace elements and oxygen isotopes data. *Goldschmidt
713 Abstracts*, 2014, 292.

- 714 Caby, R. (2003) Terrane assembly and geodynamic evolution of central-western Hoggar:
715 a synthesis. *Journal of African Earth Sciences*, 37(3), 133-159.
- 716 Caby, R., Andreopoulos-Renaud, U., and Pin, C. (1989) Late Proterozoic arc-continent
717 and continent-continent collision in the Pan-African trans-Saharan belt of Mali.
718 *Canadian Journal of Earth Sciences*, 26, 1136-1146.
- 719 Caddick, M.J., Konopásek, J., and Thompson, A.B. (2010) Preservation of Garnet
720 Growth Zoning and the Duration of Prograde Metamorphism. *Journal of*
721 *Petrology*, 51(11), 2327-2347.
- 722 Cesare, B., Ferrero, S., Salvioli-Mariani, E., Pedron, D., and Cavallo, A. (2009)
723 "Nanogranite" and glassy inclusions: The anatectic melt in migmatites and
724 granulites. *Geology*, 37(7), 627-630.
- 725 Cesare, B., Acosta-Vigil, A., Bartoli, O., and Ferrero, S. (2015) What can we learn from
726 melt inclusions in migmatites and granulites? *Lithos*, 239, 186-216.
- 727 Chernoff, C.B., and Carlson, W.D. (1997) Disequilibrium for Ca during growth of pelitic
728 garnet. *Journal of Metamorphic Geology*, 15(4), 421-438.
- 729 Clemens, J.D., and Holness, M.B. (2000) Textural evolution and partial melting of arkose
730 in a contact aureole: a case study and implications. *Visual Geosciences*, 5(4), 1-
731 14.
- 732 Dokukina, K.A., Konilov, A.N., Van, K.V., and Mints, M.V. (2017) Dumortierite- and
733 corundum-bearing quartz-feldspar-mica rocks of the Belomorian eclogite
734 province: An example of melting of phengite + quartz. *Doklady Earth Sciences*,
735 477(1), 1353-1357.
- 736 Doukkari, S.A., Ouzegane, K., Arab, A., Kiénast, J.-R., Godard, G., Drareni, A.,
737 Zetoutou, S., and Liégeois, J.-P. (2014) Phase relationships and P-T path in
738 NCFMASHTO system of the eclogite from the Tighsi area (Egéré terrane, Central
739 Hoggar, Algeria). *Journal of African Earth Sciences*, 99, 276-286.
- 740 Doukkari, S. (2016) Traitement d'images, modélisation thermodynamique et géochimie
741 des écoligites et des séries basiques de l'Egéré (Nord Hoggar). Ph.D. thesis,
742 USTHB, Algiers.
- 743 Doukkari, S.A., Ouzegane, K., Godard, G., Diener, J.F.A., Kiénast, J.-R., Liégeois, J.-P.,
744 Arab, A., and Drareni, A. (2015) Prograde and retrograde evolution of eclogite
745 from Adrar Izzilatène (Egéré-Aleksod terrane, Hoggar, Algeria) determined from
746 chemical zoning and pseudosections, with geodynamic implications. *Lithos*, 226,
747 217-232.
- 748 Duplan, L. (1967) La chaîne de l'Eg'éré (Hoggar septentrional). *Bulletin de la Société*
749 *géologique de France*, (7^{ème} série) IX, 292-297.
- 750 Duplan, L. (1972) La chaîne de l'Egéré (Hoggar septentrional). *Bulletin du Service*
751 *géologique de l'Algérie*, (nouv. sér.) 26, 57 p. + maps.
- 752 Dusel-Bacon, C., and Foster, H.L. (1983) A sillimanite gneiss dome in the Yukon
753 crystalline terrane, east-central Alaska; petrography and garnet-biotite
754 geothermometry. *Geological Survey Professional Paper* 1170-E, 25 p. US
755 government printing office, Washington.
- 756 Ferrero, S., Bartoli, O., Cesare, B., Salvioli-Mariani, E., Acosta-Vigil, A., Cavallo, A.,
757 Groppo, C., and Battiston, S. (2012) Microstructures of melt inclusions in
758 anatectic metasedimentary rocks. *Journal of Metamorphic Geology*, 30(3), 303-
759 322.

- 760 Ferrero, S., Wunder, B., Walczak, K., O'Brien, P.J., and Ziemann, M.A. (2015)
761 Preserved near ultrahigh-pressure melt from continental crust subducted to mantle
762 depths. *Geology*, 43, 447-450.
- 763 Ferrero, S., Godard, G., Palmeri, R., Wunder, B., and Cesare, B. (2018) Partial melting of
764 ultramafic granulites from Dronning Maud Land, Antarctica: Constraints from
765 melt inclusions and thermodynamic modeling. *American Mineralogist*, 103(4),
766 610-622.
- 767 Fettous, H. (2016) Le Paléoprotozoïque dans le Hoggar Occidental et central et son
768 évolution post-éburnéenne, 479 p. Ph.D. thesis, USTHB, Algiers.
- 769 Ganade de Araujo, C.E., Rubatto, D., Hermann, J., Cordani, U.G., Caby, R., and Basei,
770 M.A. (2014) Ediacaran 2,500-km-long synchronous deep continental subduction
771 in the West Gondwana Orogen. *Nature Communications*, 5, 5198 (doi:
772 10.1038/ncomms6198).
- 773 Godard, G. (2001) Eclogites and their geodynamic interpretation: a history. *Journal of*
774 *Geodynamics*, 32, 165-203.
- 775 Harte, B., Pattison, D.R.M., and Linklater, C.M. (1991) Field relations and petrography
776 of partially melted pelitic and semi-pelitic rocks. In G. Voll, J. Töpel, D.R.M.
777 Pattison, and F. Seifert, Eds. *Equilibrium and kinetics in contact metamorphism:*
778 *The Ballachulish igneous complex and its aureole*, p. 181-209. Springer Berlin
779 Heidelberg, Berlin, Heidelberg.
- 780 Hartel, T.H.D., Pattison, D.R.M., Helmers, H., and Maaskant, P. (1990) Primary
781 granitoid-composition inclusions in garnet from granulite facies metapelite: Direct
782 evidence for the presence of a melt? *Geological Association of Canada, Program*
783 *with Abstracts*, 15, A54.
- 784 Henry, D.J., and Guidotti, C.V. (2002) Titanium in biotite from metapelitic rocks:
785 Temperature effects, crystal-chemical controls, and petrologic applications.
786 *American Mineralogist*, 87(4), 375-382.
- 787 Hermann, J., and Green, D.H. (2001) Experimental constraints on high pressure melting
788 in subducted crust. *Earth and Planetary Science Letters*, 188(1), 149-168.
- 789 Hermann, J., Spandler, C., Hack, A., and Korsakov, A.V. (2006) Aqueous fluids and
790 hydrous melts in high-pressure and ultra-high pressure rocks: Implications for
791 element transfer in subduction zones. *Lithos*, 92(3), 399-417.
- 792 Holland, T., and Powell, R. (2011) An improved and extended internally consistent
793 thermodynamic dataset for phases of petrological interest, involving a new
794 equation of state for solids. *Journal of Metamorphic Geology*, 29(3), 333-383.
- 795 Holness, M.B., and Sawyer, E.W. (2008) On the pseudomorphing of melt-filled pores
796 during the crystallization of migmatites. *Journal of Petrology*, 49(7), 1343-1363.
- 797 Indares, A., and Dunning, G. (2001) Partial Melting of High-P-T Metapelites from the
798 Tshenukutish Terrane (Grenville Province): Petrography and U-Pb
799 Geochronology. *Journal of Petrology*, 42(8), 1547-1565.
- 800 Janák, M. (1999) Dehydration melting and devolatilization during exhumation of high-
801 grade metapelites: the Tatra Mountains, Western Carpathians. *Journal of*
802 *Metamorphic Geology*, 17, 379-395.
- 803 Keller, L.M., Abart, R., Wirth, R., Schmid, D.W., and Kunze, K. (2006) Enhanced mass
804 transfer through short-circuit diffusion: Growth of garnet reaction rims at eclogite
805 facies conditions. *American Mineralogist*, 91(7), 1024-1038.

- 806 Konrad-Schmolke, M., Handy, M.R., Babist, J., and O'Brien, P.J. (2005)
807 Thermodynamic modelling of diffusion-controlled garnet growth. Contributions
808 to Mineralogy and Petrology, 149(2), 181-195.
- 809 Korhonen, F.J., and Stout, J.H. (2005) Borosilicate- and phengite-bearing veins from the
810 Grenville Province of Labrador: evidence for rapid uplift. Journal of Metamorphic
811 Geology, 23(5), 297-311.
- 812 Korsakov, A.V., and Hermann, J. (2006) Silicate and carbonate melt inclusions
813 associated with diamonds in deeply subducted carbonate rocks. Earth and
814 Planetary Science Letters, 241(1-2), 104-118.
- 815 Lang, H.M., and Gilotti, J.A. (2007) Partial melting of metapelites at ultrahigh-pressure
816 conditions, Greenland Caledonides. Journal of Metamorphic Geology, 25(2), 129-
817 147.
- 818 Laporte, D., and Watson, E.B. (1995) Experimental and theoretical constraints on melt
819 distribution in crustal sources: the effect of crystalline anisotropy on melt
820 interconnectivity. Chemical Geology, 124, 161-184.
- 821 Laporte, D., Rapaille, C., and Provost, A. (1997) Wetting angles, equilibrium melt
822 geometry, and the permeability threshold of partially molten crustal protoliths. In
823 J.L. Bouchez, D.H.W. Hutton, and W.E. Stephens, Eds. Granite: From
824 Segregation of Melt to Emplacement Fabrics, p. 31-54. Kluwer Academic
825 Publishers, Dordrecht.
- 826 Lasalle, S., and Indares, A. (2014) Anatectic record and contrasting P-T paths of
827 aluminous gneisses from the central Grenville Province. Journal of Metamorphic
828 Geology, 32(6), 627-646.
- 829 Latouche, L. (1985) Les collisions intracratoniques et la tectonique tangentielle dans le
830 Pan-Africain du Hoggar central. Evolution géologique de l'Afrique. In R. Black,
831 Ed. Évolution géologique de l'Afrique, p. 143-158. CIFEG, Paris.
- 832 Lelubre, M. (1952) Recherches sur la géologie de l'Ahaggar, central et occidental (Sahara
833 Central), xi-354 + 385 p. Gouvernement général de l'Algérie, Alger.
- 834 Liégeois, J.-P. (2019) A new synthetic geological map of the Tuareg Shield: An overview
835 of its global structure and geological evolution. The geology of the Arab world—
836 An overview, p. 83-107, Springer.
- 837 Liégeois, J.-P., Navez, J., Hertogen, J., and Black, R. (1998) Contrasting origin of post-
838 collisional high-K calc-alkaline and shoshonitic versus alkaline and peralkaline
839 granitoids. The use of sliding normalization. Lithos, 45(1), 1-28.
- 840 Liégeois, J.P., Latouche, L., Boughrara, M., Navez, J., and Guiraud, M. (2003) The
841 LATEA metacraton (Central Hoggar, Tuareg shield, Algeria): Behaviour of an
842 old passive margin during the Pan-African orogeny. Journal of African Earth
843 Sciences, 37(3), 161-190.
- 844 Liégeois, J.-P., Abdelsalam, M.G., Ennih, N., and Ouabadi, A. (2013) Metacraton:
845 Nature, genesis and behavior. Gondwana Research, 23(1), 220-237.
- 846 Loomis, T.P. (1983) Compositional Zoning of Crystals: A Record of Growth and
847 Reaction History. In S.K. Saxena, Ed. Kinetics and Equilibrium in Mineral
848 Reactions, p. 1-60. Springer New York, New York.
- 849 Loose, D., Schenk, V. (2018) 2.09 Ga old eclogites in the Eburnian-Transamazonian
850 orogen of southern Cameroon: Significance for Palaeoproterozoic plate tectonics.
851 Precambrian Research, 304, 1-11.

- 852 Mahar, E.M., Baker, J.M., Powell, R., Holland, T.J.B., and Howell, N. (1997) The effect
853 of Mn on mineral stability in metapelites. *Journal of Metamorphic Geology*,
854 15(2), 223-238.
- 855 Marchildon, N., and Brown, M. (2002) Grain-scale melt distribution in two contact
856 aureole rocks: implications for controls on melt localization and deformation.
857 *Journal of Metamorphic Geology*, 20(4), 381-396.
- 858 Massonne, H.-J. (2009) Hydration, dehydration, and melting of metamorphosed granitic
859 and dioritic rocks at high- and ultrahigh-pressure conditions. *Earth and Planetary
860 Science Letters*, 288(1), 244-254.
- 861 Nahodilová, R., Štípská, P., Powell, R., Košler, J., and Racek, M. (2014) High-Ti
862 muscovite as a prograde relict in high pressure granulites with metamorphic
863 Devonian zircon ages (Běstvína granulite body, Bohemian Massif): consequences
864 for the relamination model of subducted crust. *Gondwana Research*, 25(2), 630-
865 648.
- 866 Paterson, S.R., Vernon, R.H., and Tobisch, O.T. (1989) A review of criteria for the
867 identification of magmatic and tectonic foliations in granitoids. *Journal of
868 structural geology*, 11(3), 349-363.
- 869 Perchuk, L., Korchagina, M., Yapaskurt, V., and Bakun-Czubarow, N. (2005) Some
870 high-pressure metamorphic complexes in the west Sudetes, Poland: I. petrography
871 and mineral chemistry. *Petrology* 13(5), 427-468.
- 872 Peucat, J.J., Drareni, A., Latouche, L., Deloule, E., and Vidal, P. (2003) U-Pb zircon
873 (TIMS and SIMS) and Sm-Nd whole-rock geochronology of the Gour Oumelalen
874 granulitic basement, Hoggar massif, Tuareg shield, Algeria. *Journal of African
875 Earth Sciences*, 37(3), 229-239.
- 876 Powell, R., and Downes, J. (1990) Garnet porphyroblast-bearing leucosomes in
877 metapelites: mechanisms, phase diagrams, and an example from Broken Hill,
878 Australia. In J.R. Ashworth, and M. Brown, Eds. *High-temperature
879 Metamorphism and Crustal Anatexis*, p. 105-123. Springer Netherlands,
880 Dordrecht.
- 881 Powell, R., and Holland, T.J.B. (1988) An internally consistent dataset with uncertainties
882 and correlations: 3. Applications to geobarometry, worked examples and a
883 computer program. *Journal of Metamorphic Geology*, 6(2), 173-204.
- 884 Rieder, M., Cavazzini, G., D'yakonov, Y.S., Frank-Kamenetskii, V.A., Gottardi, G.,
885 Guggenheim, S., Koval, P.W., Mueller, G., Neiva, A.M., and Radoslovich, E.W.
886 (1998) Nomenclature of the micas. *Clays and clay minerals*, 46(5), 586-595.
- 887 Rosenberg, C.L., and Handy, M.R. (2005) Experimental deformation of partially melted
888 granite revisited: implications for the continental crust. *Journal of Metamorphic
889 Geology*, 23(1), 19-28.
- 890 Sautter, V. (1985) An eclogite paragenesis from the Aleksod basement, Central Hoggar,
891 South Algeria. *Chemical Geology*, 50(1), 331-347.
- 892 Sawyer, E.W. (1999) Criteria for the recognition of partial melting. *Physics and
893 Chemistry of the Earth, Part A: Solid Earth and Geodesy*, 24(3), 269-279.
- 894 Sawyer, E.W. (2001) Melt segregation in the continental crust: distribution and
895 movement of melt in anatectic rocks. *Journal of Metamorphic Geology*, 19(3),
896 291-309.

- 897 Schmidt, M.W., Vielzeuf, D., and Auzanneau, E. (2004) Melting and dissolution of
898 subducting crust at high pressures: the key role of white mica. *Earth and Planetary*
899 *Science Letters*, 228(1), 65-84.
- 900 Spear, F.S., and Florence, F.P. (1992) Thermobarometry in granulites: pitfalls and new
901 approaches. *Precambrian Research*, 55(1), 209-241.
- 902 Tracy, R.J., Robinson, P., and Thompson, A.B. (1976) Garnet composition and zoning in
903 the determination of temperature and pressure of metamorphism, central
904 Massachusetts. *American Mineralogist*, 61(7-8), 762-775.
- 905 Tuccillo, M.E., Essene, E.J., and van der Pluijm, B.A. (1990) Growth and retrograde
906 zoning in garnets from high-grade, metapelites: Implications for pressure-
907 temperature paths. *Geology*, 18(9), 839-842.
- 908 Vernon, R.H., and Collins, W.J. (1988) Igneous microstructures in migmatites. *Geology*,
909 16(12), 1126-1129.
- 910 Vernon, R.H., and Collins, W.J. (2011) Structural Criteria for Identifying Granitic
911 Cumulates. *The Journal of Geology*, 119(2), 127-142.
- 912 Vielzeuf, D., and Holloway, J.R. (1988) Experimental determination of the fluid-absent
913 melting relations in the pelitic system. *Contributions to Mineralogy and*
914 *Petrology*, 98(3), 257-276.
- 915 Waters, D.J. (1988) Partial melting and the formation of granulite facies assemblages in
916 Namaqualand, South Africa. *Journal of Metamorphic Geology*, 6(4), 387-404.
- 917 Waters, D.J. (2001) The significance of prograde and retrograde quartz-bearing
918 intergrowth microstructures in partially melted granulite-facies rocks. *Lithos*,
919 56(1), 97-110.
- 920 Waters, D.J., and Whales, C.J. (1984) Dehydration melting and the granulite transition in
921 metapelites from southern Namaqualand, S. Africa. *Contributions to Mineralogy*
922 *and Petrology*, 88(3), 269-275.
- 923 White, R.W., Powell, R., and Halpin, J.A. (2004) Spatially-focussed melt formation in
924 aluminous metapelites from Broken Hill, Australia. *Journal of Metamorphic*
925 *Geology*, 22(9), 825-845.
- 926 Woodsworth, G.J. (1977) Homogenization of zoned garnets from pelitic schists. *The*
927 *Canadian Mineralogist*, 15(2), 230-242.

928 **FIGURE CAPTIONS**

929 **Figure 1.** Geological context. (a) Geological sketch map of the Tuareg Shield (Black
930 et al. 1994; Liégeois 2019). (b) Geological map of the LATEA metacraton (after Liégeois
931 et al. 2003), showing the area studied. Ao: Aouilène; As-Is: Assodé-Issalane; Az: Azrou
932 n'Fad; Eg-Al: Egéré-Aleksod; La: Laouni; Se: Serouenout; Te: Tefedest; Tz: Tazat;
933 HKCA: high-potassium calc-alkaline rocks.

934 **Figure 2.** Outcrop photographs. (a) Upper metasedimentary unit of Egéré showing
935 metapelites interbedded with marbles, quartzites and eclogite lenses (hills on the
936 horizon). (b-d) Close-up views of the migmatitic metapelites studied, showing the
937 alternation of various lithologies, in particular of leucosomes and melanosomes rich in
938 garnet porphyroblasts, kyanite and phengite (d).

939 **Figure 3.** Mineral assemblages and microtextures of kyanite-bearing metapelites.
940 Plane-polarized (b-e, g, h) and cross-polarized (a, f) lights. **(a)** Garnet megacryst, rich in
941 inclusions defining a straight internal foliation and corroded by aggregates of biotite +
942 plagioclase (Bt₃+Pl₃). **(b-d)** Close-up views of various inclusions (Bt₁, Ilm₁, Qz₁, St₁, Rt₁)
943 in garnet porphyroblasts (Grt₁), some of which are surrounded by a plagioclase moat (Pl
944 in c). **(e)** Garnet + quartz skeletal intergrowth. **(f)** Phengite flake (Ph₂), partially resorbed
945 by aggregates consisting of biotite (Bt₃), plagioclase (Pl₃) and K-feldspar (Kfs₃). **(g)**
946 Symplectite mainly consisting of Bt₃, Pl₃, Kfs₃, Sil₃ and St₃, developed at the expense of
947 the peak paragenesis, in particular Grt₂, Ph₂, Ky₂ and Qz₂. **(h)** Second generation of fine-
948 grained staurolite (St₃) associated with late Bt₃, Kfs₃ and Sil₃.

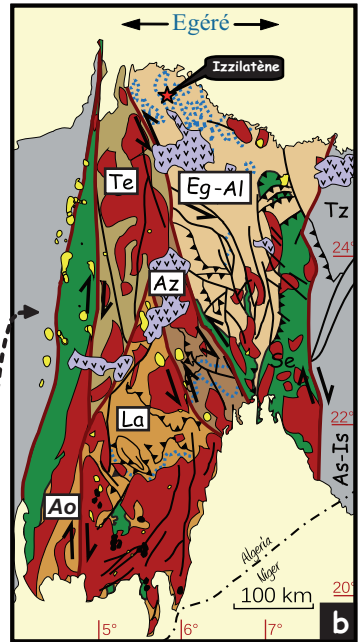
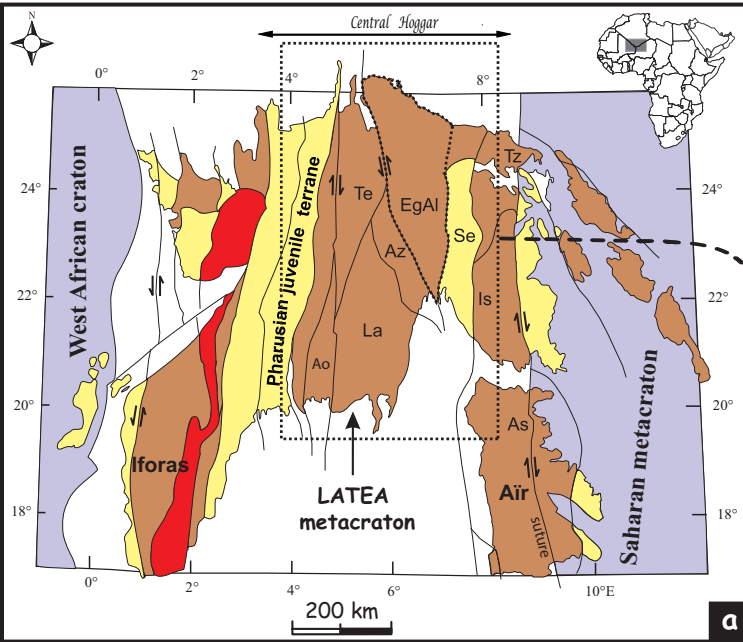
949 **Figure 4.** Reaction microstructures in kyanite metapelites. BSE images (a-e), and
950 RGB image (f), the red, green and blue channels of which are the first three main
951 components of the PCA of element maps. **(a)** The HP paragenesis (M₂), consisting of
952 garnet (Grt₁₋₂), phengite (Ph₂), kyanite (Ky₂) and quartz, is partially replaced by late M₃
953 assemblages (Bt₃+Pl₃). **(b)** Garnet megacryst (Grt₁₋₂) corroded by Bt₃+Pl₃ aggregates. **(c)**
954 Close-up view of quartz inclusions (Qz₁) in a garnet porphyroblast (Grt₁), which are
955 surrounded by thin films of plagioclase (Pl). **(d)** Aggregates of Bt₃, Pl₃, Sil₃, St₃ and Ms₃,
956 having replaced the M₂ paragenesis (Ph₂+Ky₂+Grt₂+Qz₂); K-feldspar Kfs₃ mainly
957 developed as coronas around large Qz₂ grains. **(e, f)** Phengite flake (Ph₂) partially
958 resorbed by aggregates consisting of Bt₃, Pl₃, Ms₃ and Kfs₃, which forms a continuous
959 corona at contacts with Qz₂; lamellae of Ilm₃ and Bt₃ are exsolved parallel to the (001)
960 plane of phengite Ph₂; 1: numerous micro-inclusions of ilmenite inside muscovite (*i.e.*,
961 Ms₃+Ilm₃) after Ph₂, which was probably richer in Ti near Ilm₂; 2: Pl₃+Ilm₃ symplectite
962 between Ilm₂ and Ph₂.

963 **Figure 5.** Nanogranitoids in garnet porphyroblasts. Plane-polarized light (a) and BSE
964 (b-f) images (sample T100). **(a)** Garnet megacrysts in a matrix with leucosomes and
965 micaceous segregations. **(b)** Very small melt inclusions hosted in a garnet porphyroblast
966 (Grt₁) and now crystallized as “nanogranitoids”. **(c-f)** Close-up views of
967 “nanogranitoids”, which generally display the negative euhedral forms of the host garnet
968 (d-f) and consist of quartz + biotite + plagioclase ± K-feldspar ± zircon.

969 **Figure 6.** Mineral compositions of the metapelites. **(a-d)** Composition of garnet in
970 samples T78 (a-b) and T138 (c-d). The profiles across garnet megacrysts (a, c) show a
971 smoothed compositional zoning at their cores, where a bell-shaped Mn profile is
972 observed; the zoning at the rims of profile (a) is similar to that of the inner rims of profile
973 (b), whose outer rims show a reverse zoning when at contact with Bt₃+Pl₃ symplectites.
974 **(e)** White mica compositions in the diagram (Si+Fe²⁺+Mg) vs. (Al^{IV}+Al^{VI}), showing the
975 phengite substitution (Si₊₁[Fe²⁺,Mg]₊₁+Al^{IV}₋₁Al^{VI}₋₁). **(f)** Staurolite compositions in the
976 diagram X_{Mg}-Si. **(g)** Biotite compositions (diagram of Rieder et al. 1998). **(h)** Feldspar

977 compositions. The symbols and colors in (g) and (h) represent microstructural sites and
978 samples, respectively (see the common legend).

979 **Figure 7.** *P-T* pseudosections for samples T78 and T52. Notations used for the
980 isopleths: $x(Grt/Bt/St) = (Fe/(Fe + Mg))$; $z(Grt) = (Ca/(Ca + Fe + Mg + Mn))$; $Si(Ph) = Si$.
981 The presumed prograde and retrograde *P-T* paths (red dashed curves) are constrained by
982 various isopleths and isomodes; the blue dashed arrows indicate the shift of the solidus
983 curve towards higher temperatures during melt extraction (see text).



- Juvenile Pan-African terranes
- Paleoproterozoic terranes remobilized during the Pan-African orogeny
- Archean terranes remobilized during the Pan-African orogeny
- Craton-metacraton

- Cenozoic volcanism
- Phanerozoic sediments
- 580-525 Ma a/c-calc plutons
- Mafic-ultramafic layered complexes
- 630-580 Ma HKCA batholiths
- Pan-African eclogites
- juvenile terranes (Neoproterozoic)
- Non-LATEA terranes
- Eburiian basements of LATEA terranes
- ★ Location of the investigated samples from Izzilatène area

Figure 1

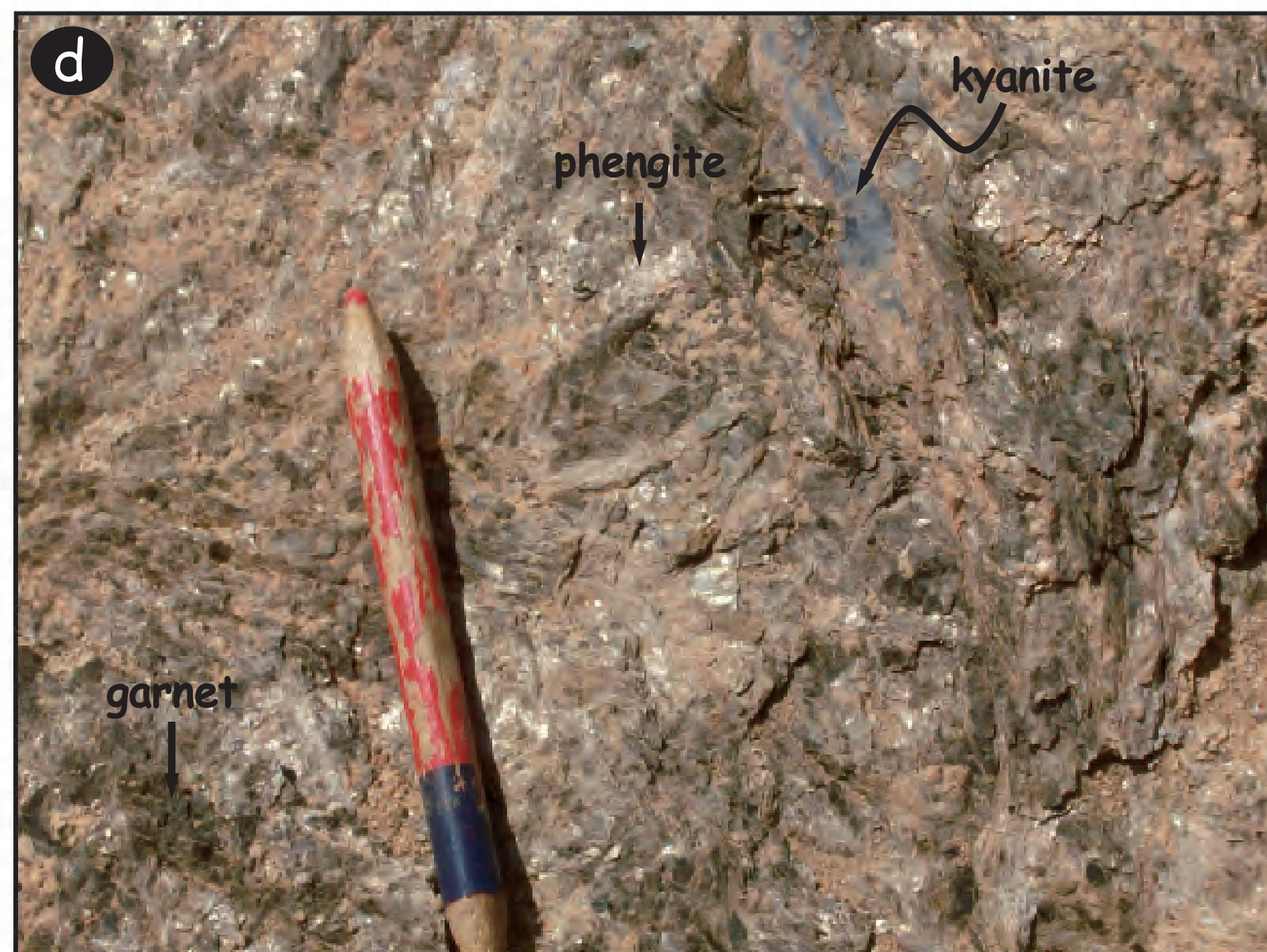
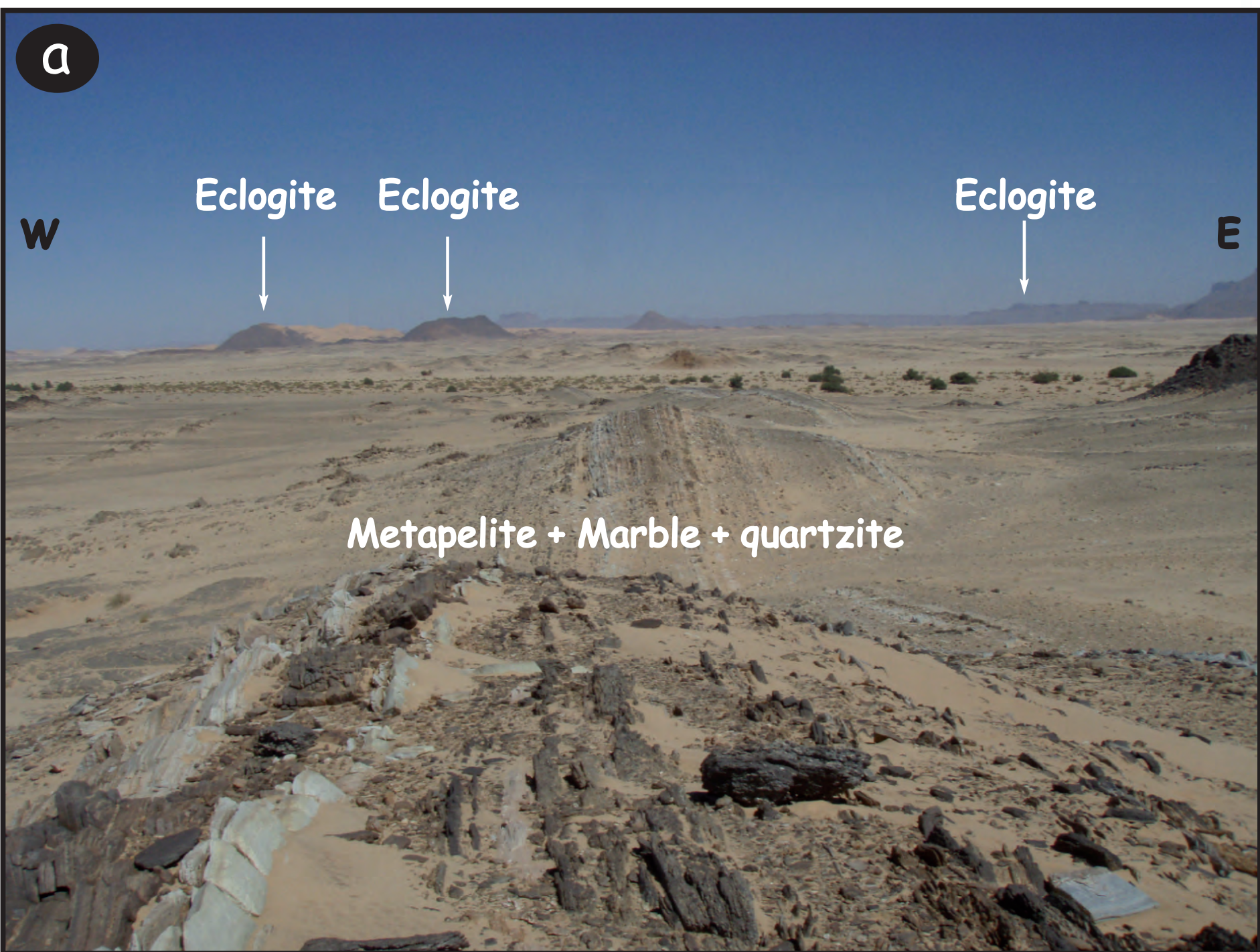


Figure 2

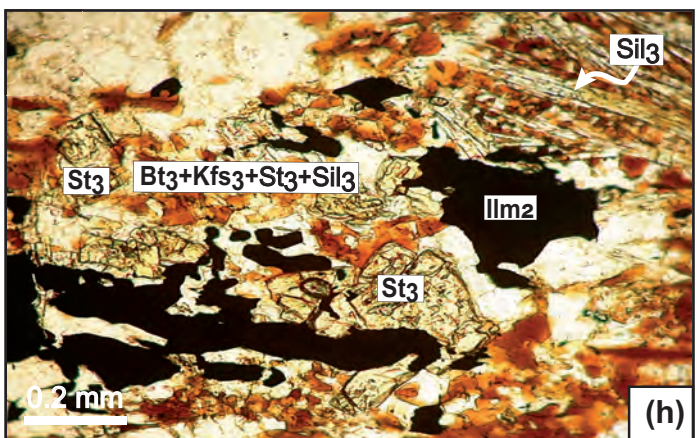
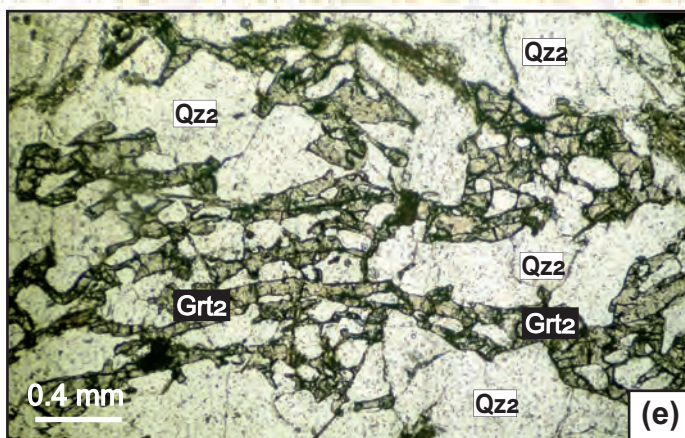
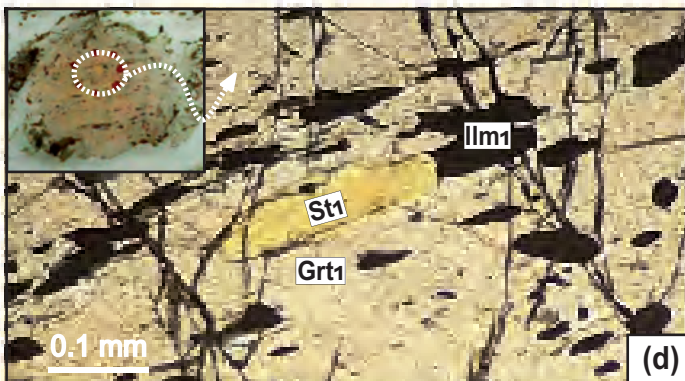
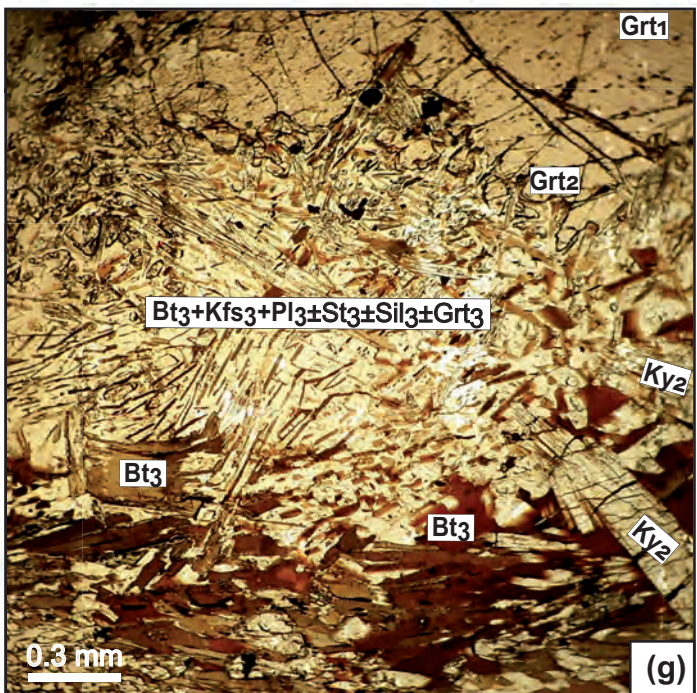
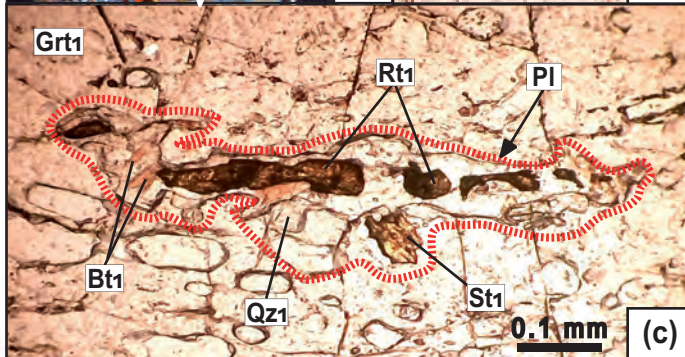
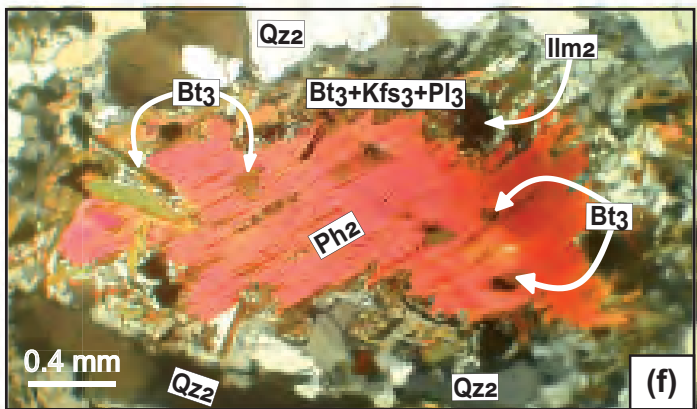
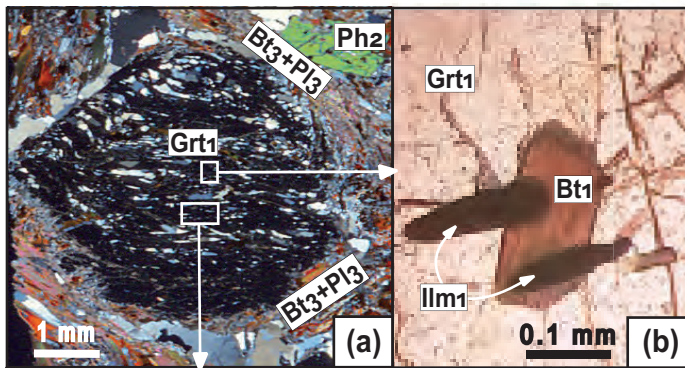


Figure 3

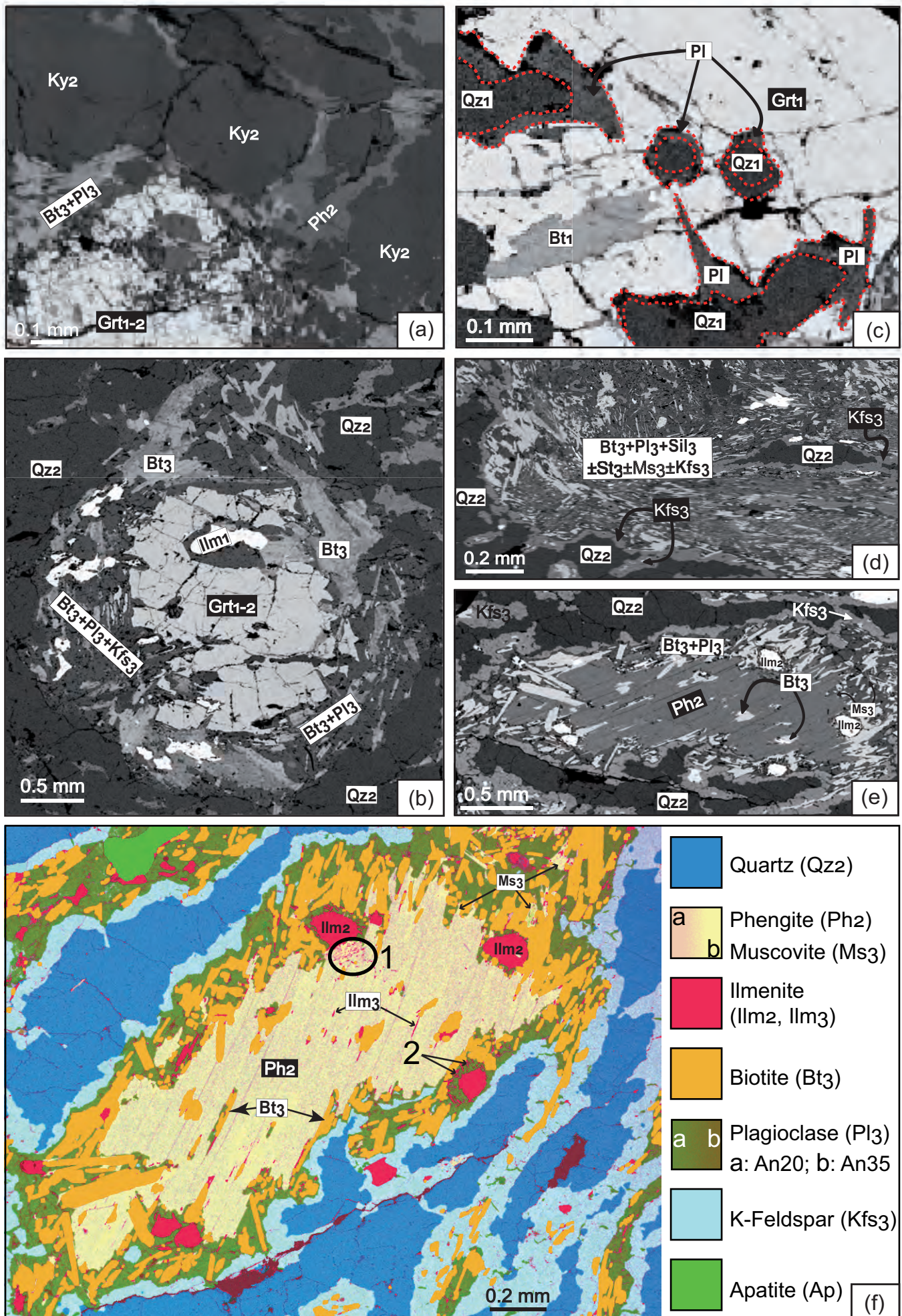


Figure 4

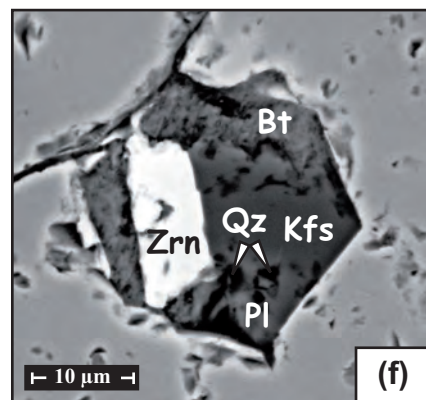
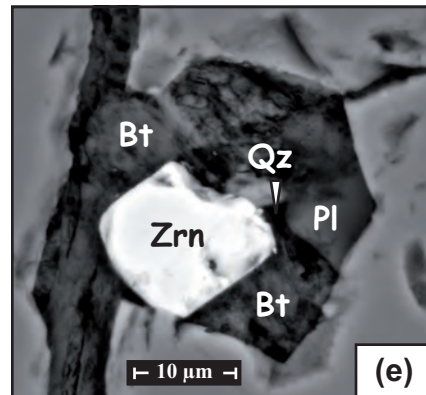
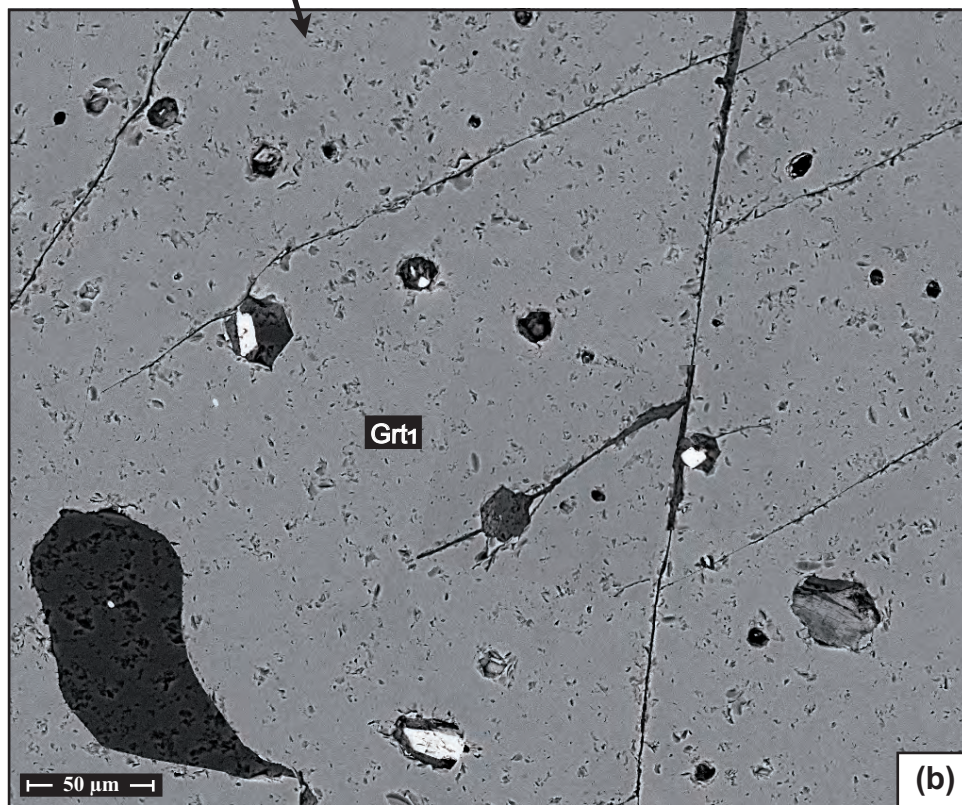
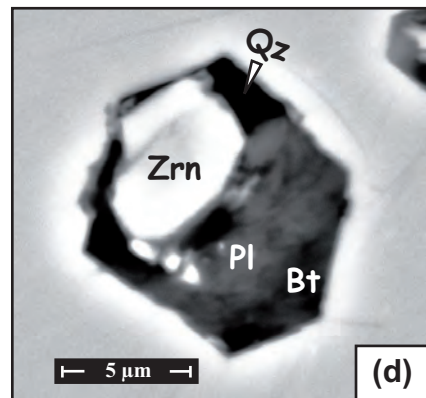
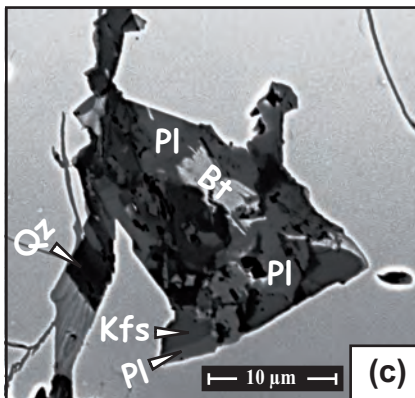
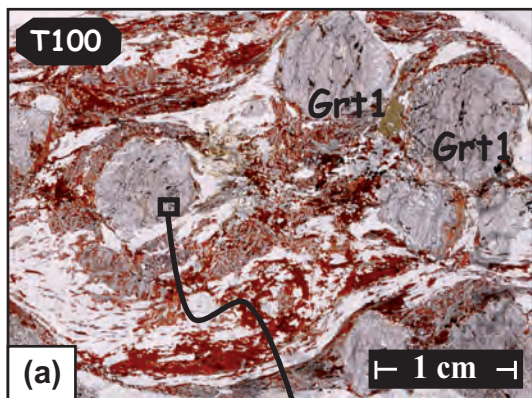


Figure 5

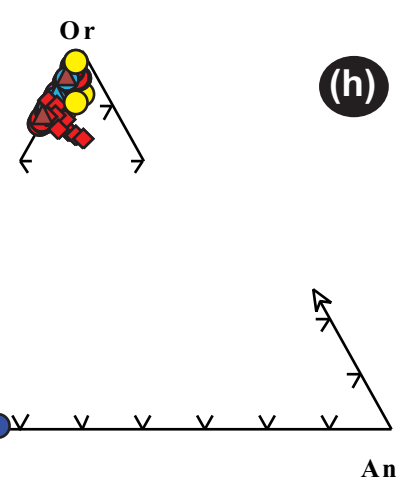
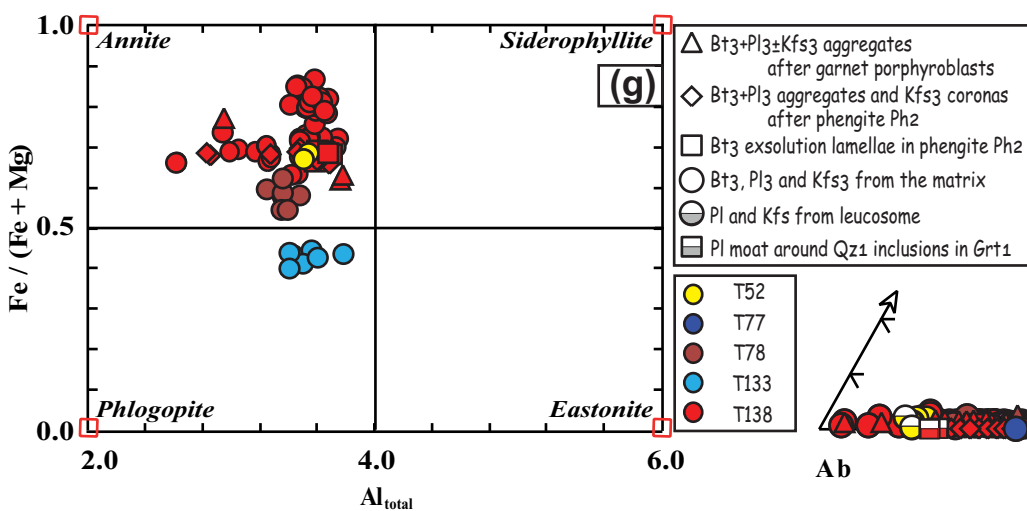
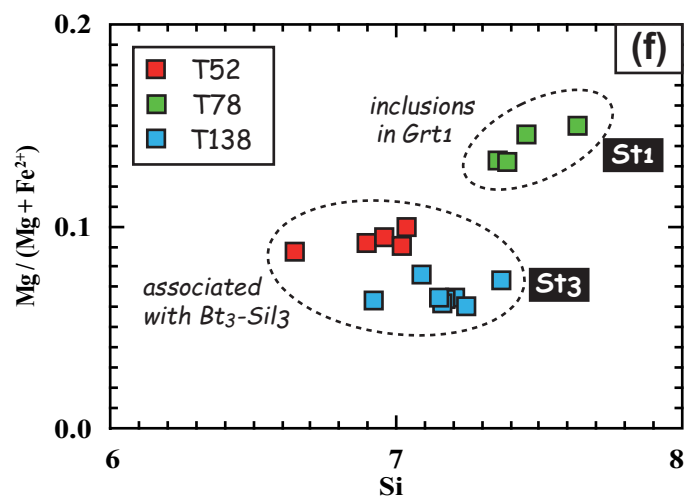
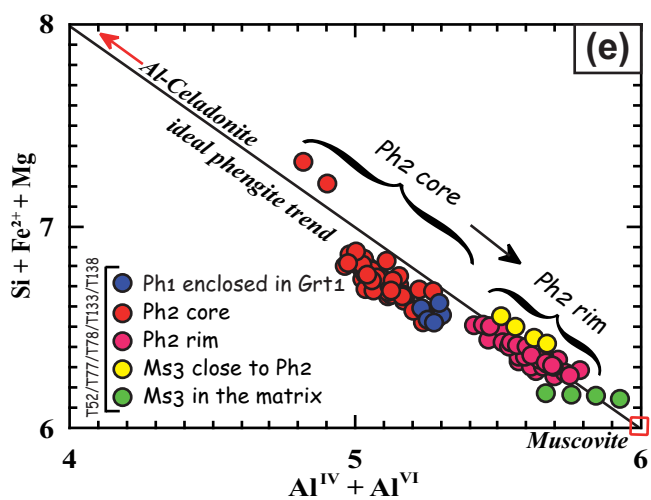
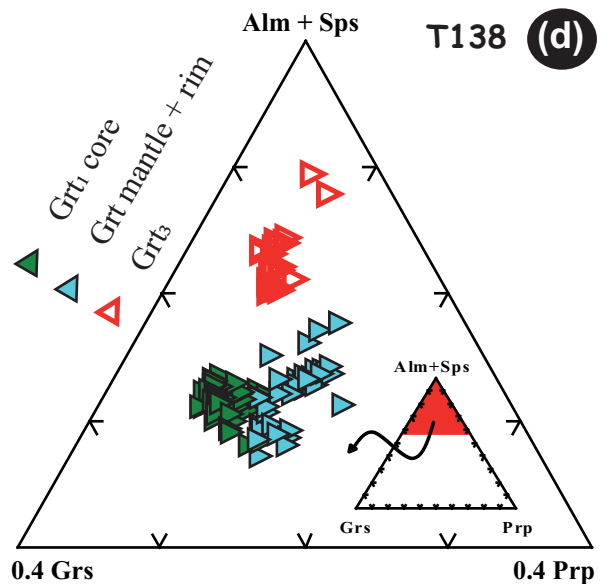
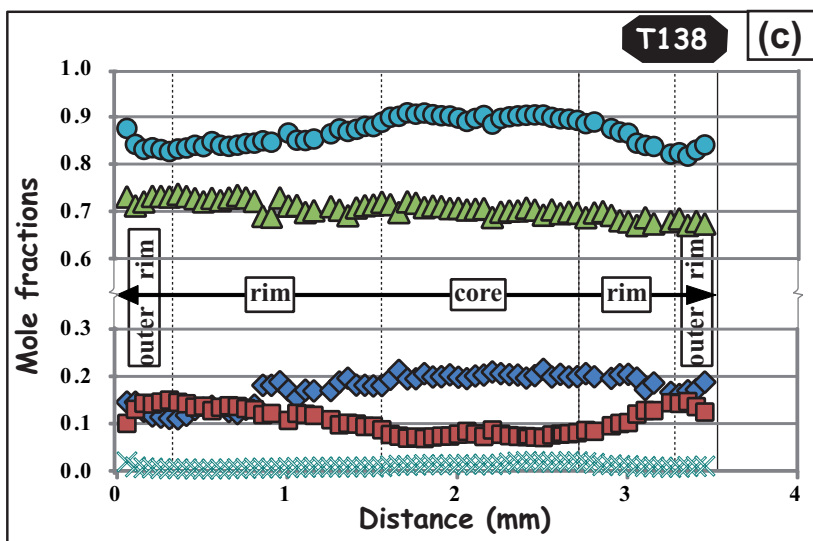
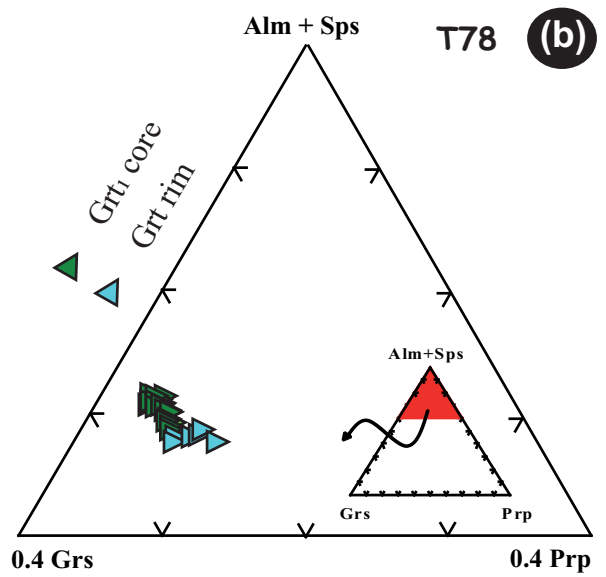
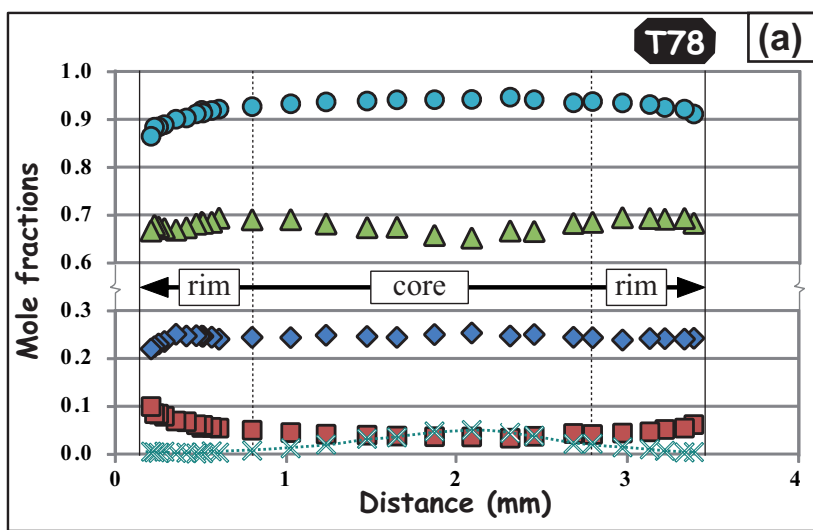


Figure 6

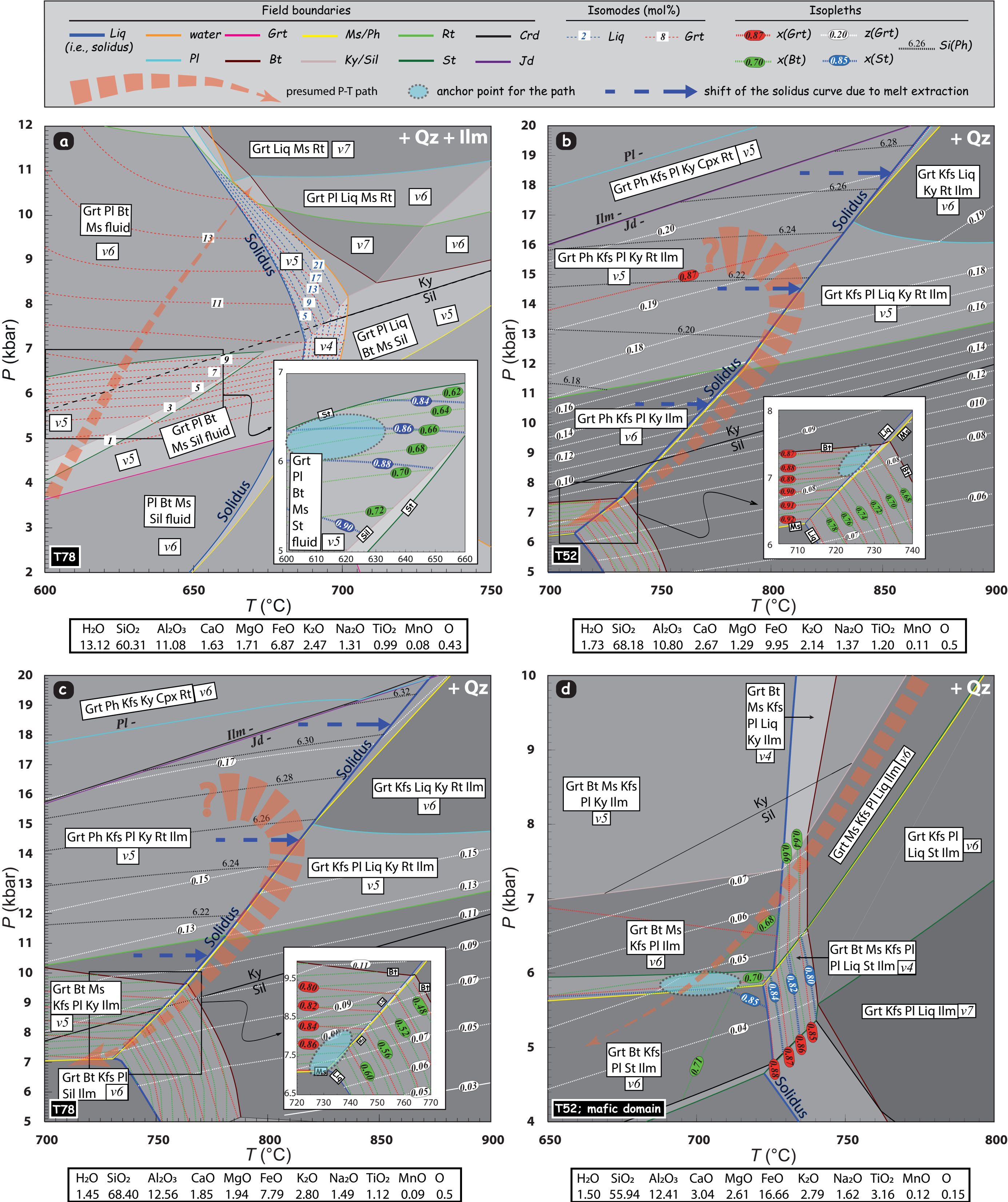


Figure 7